~~Satellite Observations Reveal~~ A Semi-direct Effect from Northern California ~~Wildfire~~ Biomass Burning Aerosols ~~Reduce~~ Contributes to Decreased Cloud Cover ~~in California and Nevada Through Semi-Direct Effects~~over the Region

James L. Gomez[1], Robert J. Allen[1], and King-Fai Li[2]

[1]Department of Earth & Planetary Sciences, University of California Riverside, Riverside, USA
[2]Department of Environmental Sciences, University of California Riverside, Riverside, USA

Correspondence: James Gomez (jgome222@ucr.edu)

Abstract. Wildfires in the southwestern United States, particularly in northern California (nCA), have grown in size and severity in the past decade. As they have grown larger, they have been associated with large emissions of absorbing aerosols ~~in to~~ and heat into the troposphere. Utilizing satellite observations from MODIS, CERES, ~~AIRS~~and AIRS, as well as reanalysis from MERRA-2, ~~and CALIPSO,~~ the meteorological effects of aerosols associated with fires during the wildfire season (June-October) were discerned over the nCA-NV (northern California and Nevada) region in the 2003-2022 time ~~frame. As higher temperatures and low~~ period. Wildfires in the region have a higher probability of occurring on days of positive temperature T anomalies and negative relative humidity RH ~~dominate during high surface pressure p_s atmospheric conditions, the effects of the aerosols on high~~ anomalies, making it difficult to discern the radiative effects of aerosols that are concurrent with fires. To better isolate the effects of large fire emissions on meteorological variables, such as clouds and precipitation, variable anomalies on high fire emission days (90th percentile) ~~fire days~~ were compared to low fire emission days (10th percentile) ~~days were~~ and were further stratified based on whether ~~p_s~~ surface relative humidity RH_s was anomalously high ~~or anomalously low (10th percentile) . An increase in tropospheric temperatures was~~ (75th percentile) or low (25th percentile) compared to typical fire season conditions. Comparing the high fire emission/high RH_s data to the low fire emission/high RH_s data, positive tropospheric T anomalies were found to be concurrent with ~~more absorbing aerosol aloft, which is~~ positive AOD anomalies, which was associated with significant ~~reductions in tropospheric~~ negative 850 hPa-300 hPa RH ~~during both 90th and 10th percentile p_s~~ anomalies during both 75th percentile RH_s conditions. Furthermore, high fire ~~days under low p_s~~ emission days under high RH_s conditions are associated with ~~reduced cloud fraction~~ negative CF anomalies that are concurrent with the negative RH anomalies, which is consistent with the traditionally-defined aerosol-cloud semi-direct effect. ~~The reduced~~ This negative CF ~~, in turn,~~ anomaly is associated with ~~reduced TOA SW radiative flux , a warmer surface, and less precipitation. These changes could~~ a significantly negative regional precipitation anomaly and an positive net top of atmosphere radiative flux anomaly (a warming effect) in certain areas. The T, RH, and CF anomalies under the high fire emission/high RH_s conditions compared to low fire/high RH_s conditions correlate significantly spatially with AOD anomalies. Additionally, the vertical profile of these variables under the same stratification are consistent with positive black carbon mass mixing ratio anomalies

from MERRA-2. As a result, large fires in California may create a positive feedback that could intensify fire weather, and therefore extend fire lifetime and impacts.

1 Introduction

As a result of climate change, land use change, and forest management, ~~frequency and severity~~ the frequency of wildfires in ~~the southwestern Unites States (US) have trended upwards over the last decade (Li & Banerjee, 2021; Brown et al., 2023), and~~ California has trended upward from 100 fires per year in the 1920s to 300 fires per year in the late 2010s (Li & Banerjee, 2021) . The size of these wildfires has also increased, with total burned area (square distance burned by a fire) increasing from roughly 1000 km^2 to almost 4000 km^2 in the same time period (Li & Banerjee, 2021). According to a recent study, frequency of extreme daily wildfire events in the region are projected to increase by 59%-172% in coming years due to ~~intensified drought and heatwaves (Goss et al., 2020; Palinkas, 2020; Ager et al., 2021; United Nations Environment Programme, 2022)~~ climate change (Brown et al., 2023), which is consistent with findings of numerous other studies (Palinkas, 2020; Ager et al., 2021; United . In both higher and lower CO_2 mitigation scenarios, large wildfire events are projected to become more commonplace by the end of the 21st century worldwide, as well in the southwestern US (United Nations Environment Programme, 2022). Large wildfire events in the late 2010's and early 2020's ~~, known as "mega-fires",~~ were associated with more intense "fire weather": high temperatures T, low relative humidity RH, and high surface wind speeds U_s (Varga et al., 2022; Keeley & Syphard, 2019). These fire weather conditions may be potentially intensified, or alleviated, by the fires themselves. ~~As fires combust vegetation, they emit biomass burning (BB) aerosols such as black carbon (BC), organic aerosols (OA), and brown carbon.~~ Higher burn severity wildfires, such as the 2020 wildfires in California (CA), have been observed to inject smoke plumes higher into the troposphere than in previous years (Wilmot et al., 2022). These smoke plumes consist of both shortwave (SW) absorbing aerosols such ~~BC~~ black carbon BC and reflective aerosols such as ~~OA~~organic aerosol (OA), as well as brown carbon, which is ~~both~~ absorbing and reflective. Additionally, ~~they may contain other aerosols aside from BB aerosols, such as dust (Wagner et al., 2021, 2018), which also has SW absorbing properties (Highwood & Ryder, 2014).~~ wildfires have also been associated with emission of other aerosol species through feedbacks. While dust is not emitted from biomass burning, a number of studies have linked fires to concurrent dust emission through creation of convective updrafts (Wagner et al., 2018, 2021) and delayed dust emissions through wildfire clearing of vegetation (Wagenbrenner et al., 2013, 2017; Yu & Ginoux, 2022). The absorbing properties of wildfire smoke and co-emitted dust over the western US, measured using absorbing aerosol optical depth (AAOD), is uncertain. However, a recent study of CA fires indicates that wildfires increase AAOD relative to the annual mean by tenfold (Cho et al., 2022). An injection of absorbing aerosols into the troposphere may cause a local warming affect, altering the hydrological and radiative balance of the atmosphere (Allen & Sherwood, 2010; Thornhill et al., 2018; Allen et al., 2019; Herbert & Sti . Smoke plumes that reach the upper troposphere (pressures$<$500 hPa) may deposit absorbing aerosols that could burn off high clouds, and promote more stable low clouds (Stjern et al., 2017; Smith et al., 2018; Allen et al., 2019), leading to SW and longwave (LW) cooling~~, an effect also observed to occur with methane SW absorption (Allen et al., 2023)~~. Alternatively, if the absorbing aerosols are concurrent with low clouds, the relative humidity of the liquid cloud layer would be decreased, burning off low clouds and leading to ~~increased SW forcing~~ a decrease in outgoing SW flux (Koch & Del Genio, 2010; Allen & Sherwood, 2010). ~~Additionally, the higher injection~~ These are both examples of aerosol semi-direct effects. Past observations and modelling experiments have shown dust aerosol is associated with semi-direct effects (Tsikerdekis et al., 2019; Amiri-Farahani et al., 2017; , as dust also has SW absorbing properties (Highwood & Ryder, 2014; Kok et al., 2023). Furthermore, the higher altitude of absorbing aerosol from California fires may alter cloud microphysics, which also has the potential to change the radiative balance of the surface and atmosphere. An influx of aerosols into the troposphere may create an abundance of cloud condensation nuclei (CCN) for droplets to condense onto, decreasing effective radius R_{eff} of the clouds, an effect already observed with smoke (OA ~~/BC~~and BC) particles in the northwestern US (Twohy et al., 2021). A decrease in R_{eff} would increase the albedo of the clouds, assuming constant water path, which would then increase outgoing SW radiation. This decrease in R_{eff} can also affect liquid water path LWP as the smaller droplets can evaporate much faster than larger droplets, or the smaller droplets can suppress precipitation, which increases LWP by reducing the liquid water leaving the cloud (Goren & Rosenfeld, 2012). The lighter droplets can also be lofted higher in the atmosphere, where they condensate further and release latent heat, then eventually fall from this greater height and evaporate. Therefore, to compensate, polluted clouds have more intense updrafts and downdrafts than pristine clouds (Khain, 2009). SW absorption itself can also decrease precipitation P in other ways, such as reducing SW radiation reaching the surface or through rapid atmospheric adjustments (Sand et al., 2020; Samset, 2022; Allen et al., 2023).

Large Fires are not only limited to the western US. Australia, the Mediterranean Basin, and South America have all experienced an increase in large fire events due to climate change and land management (Shi et al., 2021; Ruffault et al., 2020; Artaxo et al., 2013; Allen . As the western US, and other parts of the world, enter this new regime of ~~mega-fires~~large fires, there comes a need for improved understanding of the effects of aerosols ~~primarily and secondarily emitted~~ emitted primarily (through biomass burning), secondarily (oxidation of emitted volatiles), or through feedbacks (such as dust emissions concurrent with fires) by wildfires. Models participating in the Coupled Model Intercomparison Project version 6 (CMIP6) (Eyring et al., 2016) do not have parametrizations of ~~BB~~ biomass burning (BB) aerosol emissions that respond to CO_2 emissions in most of their experiments, including the DECK (Diagnosis, Evaluation, and Characterization of Klima) experiments (Gomez et al., 2023). ~~Instead, modellers~~ The models that have interactive BB aerosol emissions tend to parameterize them as a function of fuel flammability (temperature and moisture), fuel density, and plant functional type (Mangeon et al., 2016; Li et al., 2019). Most models participating in CMIP6 do not have dynamic vegetation models (Li et al., 2019), and therefore are incapable of incorporating fire-dust feedbacks. Instead, modelers rely on prescription of BB aerosols in ~~these experiments.~~most experiments.

Recent modelling experiments have found significant effects of wildfires on regional and global climate scales. Previously, using prescribed aerosol simulations in the Community Earth System Model version 2 (CESM2), it was ~~hypothesized~~ shown that the large 2019 wildfires in Australia could have intensified that year's La Niña through aerosols directly cooling the ocean surface (Fasullo et al., 2021). Another CMIP6 study observed a similar effect on La Niña as a result of a teleconnection caused by an influx of absorbing aerosols into the atmosphere from South African wildfires (Amiri-Farahani et al., 2020). Biomass burning aerosols may also have other effects on large scale ocean circulation, such as an invigoration of the Atlantic Meridional

Overturning Circulation (Allen et al., 2024b). As far as the southwestern US is concerned, a modeling experiment using the WRF/CHEM model was run to analyze the effects of a wildfire event on weather forecasts (Chen et al., 2014). This study found that the BB aerosols suppressed convection, prevented cloud formation, and decreased precipitation. While studies such as these demonstrate that it is possible to model past effects of fires on local and global climate, without ~~proper~~ parameterization of BB aerosol emission, as well as parametrization of secondary dust aerosol emission from wildfire-cleared vegetation, the radiative forcing of future fires' primary and secondary aerosols will remain a source of uncertainty. ~~Therefore,~~ Furthermore, there are few, if any studies, that attempt to discern the impacts of large fires over the southwestern US. Twohy et al. (2021) analyzed satellite observations of cloud microphysical properties over part of the region, however this study was conducted during only one wildfire event in 2018. As a result, there is no comprehensive long-term observational study over the southwestern US concerning wildfire aerosol-cloud interaction. Therefore, to ~~further motivate the need to incorporate interactive aerosol emissions from wildfires in climate models, as well as to~~ further understand the effects of wildfires on the climate of one of the most populated areas in the US, this paper aims to quantify the radiative as well as microphysical effects that these aerosols have in the region under different atmospheric conditions utilizing satellite data.

2 Satellite and ~~Other Observational Data~~Reanalysis Datasets

The objective of this ~~analysis is to determine how cloud properties differ as a result of primary and secondarily emitted wildfire aerosols~~ study is to quantify the impacts of wildfire aerosol emissions on meteorological parameters, such as clouds and precipitation, over the southwestern US using ~~satellite observationsfrom the Aqua and Cloud-Aerosol Lidar and Infrared Pathfinder Satellite Observation (CALIPSO) (Winker, 2019; Tackett et al., 2018) satellites, as well as fire~~ observations. This includes the Aqua satellite with the MODIS, AIRS and CERES instruments. The Modern-Era Retrospective analysis for Research and Applications, Version 2 (MERRA-2) reanalysis project (Randles et al., 2017; Global Modeling And Assimilation Office & Pa is used to obtain daily black carbon mass mixing ratio vertical profiles. Fire dry matter emission data DM are used as a proxy for fire severity, and are derived from the Global Fire Emissions Database ~~(GFED~~version 4 (GFED4) (van der Werf et al., 2017; Randerson et al., 2017). All data sets are ~~level 3 globally gridded~~ globally gridded observational data sets, with the exception of ~~GFED which is considered a level 4 globally gridded dataset.~~ GFED4 and MERRA-2 which are considered globally gridded reanalysis datasets.

2.1 Global Fire Emissions Database (~~GFED~~GFED4)

~~GFED~~ GFED4 DM emissions are calculated in the Carnegie–Ames–Stanford Approach (CASA) model, which requires MODIS burned area data, meteorological data from the ERA-Interim reanalysis dataset, ~~photsynthetically~~ photosynthetically active radiation data based on Advanced Very ~~High Resolution~~ high-resolution Radiometer satellite instrument retrievals, and vegetation continuous fields data from the MODIS MOD44B dataset (van der Werf et al., 2017). ~~The~~ DM is the emission of any gas or aerosol from burned vegetation, and a list of all these types of emission can be found in van der Werf et al. (2017) . The CASA model is run using burned area data from combined MODIS-Aqua and MODIS-Terra level 3 data (MCD64A1).

Wildfire studies tend to either use fire power (from MODIS or VIIRS) or burned area-based datasets to quantify fire severity. Burned area is determined by MODIS from a time series of burn sensitive vegetation index, which compares daily surface reflectances (Giglio et al., 2018). Fire power is the radiated energy from fires over time, and MODIS determines this quantity by comparing the brightness temperature of a fire pixel to the background brightness temperature (Peterson et al., 2013). Use of a burned area based area-based dataset is preferable to a fire power dataset for this paper, as cloud cover may obstruct fire power data retrievals, leading to an underestimation of fire size/severity on a given day. This underestimation in a given time period. While cloud cover can also block burned area retrievals, burned area can be recorded once cloud cover has been dissipated, unlike fire power. This introduces a temporal uncertainty, however. This temporal uncertainty is $\pm$1 day for clear sky conditions, $\pm$5 days under consistent 75% cloud cover, and up to $\pm$20 days over persistently very cloudy (85% or higher) intervals (Giglio et al., 2013). However, this temporal uncertainty is likely of little significance for this paper, as cloud cover over the western US during the wildfire season is rarely persistently high (aside from "June gloom" in coastal regions), and the lifetime of biomass burning aerosols (roughly 4-12 days) is generally greater than or equal to the temporal uncertainty of clear sky or consistently cloudy burned area data (Cape et al., 2012). The daily underestimation of fire power is demonstrated in **Figure S2S1**, which indicates that Aqua fire power retrievalsunderestimate , taken from the MYD14A1 dataset (Giglio & Justice, 2015), underestimate daily fire severity compared to DM with 98% of days reporting a lower normalized fire power than normalized DM. Therefore, for fire power to be a more useful metric, a daily combined Aqua/Terra/VIIRS dataset would have to be used, which is not available for the time frame period of interest. GFED GFED4 fire emissions are also preferred over fire power data and raw burned area data as calculation of fire emissions takes vegetation type and net primary production into account. Raw burned area and fire power datasets yield information about fire size and intensity, but as aerosol emission also depends on the type of vegetation being burned, use of either dataset over a fire emissions dataset may under-estimate or over-estimate biomass burning aerosol impacts on clouds. However, use of GFED GFED4 data has drawbacks. While use of burned area data reduces the chance of an underestimation of fire impacts, a the previously mentioned temporal uncertainty is introduced. This temporal uncertainty is $\pm$1 day for clear sky conditions, $\pm$5 days under consistent 75% cloud cover, and up to $\pm$20 days over persistently very cloudy (85% or higher) intervals (Giglio et al., 2013). However, this temporal uncertainty is likely of little significance for this paper, as cloud cover over the western US during the wildfire season is rarely persistently high (aside from "June gloom" in coastal regions), and the lifetime of biomass burning aerosols (roughly 4-12 days) is generally greater than or equal to the temporal uncertainty of clear sky or persistently cloudy burned area data (Cape et al., 2012). Additionally, as the output from GFED is from an older model, which may introduce additional uncertaintyAdditionally, the CASA model itself is associated with uncertainties. Calculation of net primary production in the model, for example, does not take meteorological variables into account (Liu et al., 2018). As a result, caution must be taken when analyzing the results. To ensure results are accurate, the GFED robust, the GFED4 DM stratification method was verified by analyzing MODIS AOD anomalies (see Section 2.2) during large fire events (Section 3.3, Section 4.2), and by performing cross correlations between AOD and DM (Supplement section 1). GFED , **Figure S2**). GFED4 emissions and burned area data are available from 1997-2016. Data for 2017-2022 is also available, but the data is in "beta" and therefore is more limited. Both the complete and the beta data contain total carbon emissions, as well as dry matter emission. GFED GFED4 also estimates the contribution of 6 different types of vegetation biomes (boreal forest, temperate forest, grassland, agriculture, and peat) to the carbon and dry matter emissions. However, the beta dataset only estimates these contributions for DM. Therefore, DM is used as a proxy for the severity of a given fire's emissions, as it is the only variable that both the complete and beta data contain and speciate. All ~~other~~ observational datasets utilized in this ~~project~~ study have a 1^o resolution, however ~~GFED~~ GFED4 emission data is of a 0.25^o resolution. Therefore, this data was regridded to a 1^o grid. It should be noted that GFED5 has recently been released (Chen et al., 2023), however this dataset was not used as it does not yet include emissions, only has data available up to 2020, and was released after analysis for this paper had concluded.

2.2 Aqua

MODIS-Aqua: Cloud and aerosol optical depth (AOD) data were derived from Moderate Resolution Imaging Spectroradiometer (MODIS) level 3 data. Specifically, the MODIS collection 6.1 1^o level 3 product (MYD08_D3) (Platnick et al., 2003; Salomonson et al., 2002; MODIS Atmosphere Science Team, 2017) is utilized, which yields daily retrieval products from the Aqua satellite. The Aqua satellite makes two overpasses for the region of interest: one ascending run from 2-3 PM, and one descending run from 2-3 AM. The descending dataset is used as most MODIS level 3 cloud property products provided are descending (morning) only. For MODIS cloud retrievals during periods of large AOD, especially when the aerosols are concurrent with clouds, it is possible for MODIS to misidentify aerosols as clouds (Herbert & Stier, 2023). This may cause errors in cloud property retrievals, as well as an overestimation of cloud fraction CF. This may lead to overestimation of CF during anomalously large fire events. While the MODIS Dark-Target and Deep Blue AOD algorithms are extensively quality controlled and evaluated (Levy et al., 2013; Platnick et al., 2017; Wei et al., 2019), there is still room for errors in AOD and cloud retrieval. Additionally, as it is not possible to distinguish wildfire AOD from other AOD, whenever possible, fire emissions from ~~GFED~~ GFED4 are used to discern the impacts of fires on cloud properties.

AIRS: Data concerning T, water mass mixing ratio M_{H_2O}, CF, and RH profiles, as well as surface temperature T_s and surface relative humidity RH_s, were derived from Atmospheric Infrared Sounder (AIRS) level 3 daily data (AIRS3STD) (AIRS Science Team & Texeira, 2013). ~~AIRS collects data on an ascending (morning) a descending (afternoon/evening) overpass. For this paper, the descending data was used as it is more temporally consistent~~ As with the MODIS ~~derived cloud properties, and the data was associated with lower standard errors than the ascending data for the region of interest~~data, the descending dataset is used.

CERES: Top of atmosphere as well as in-atmosphere radiative flux data was derived from Clouds and the Earth's Radiant Energy System (CERES) level 3 ~~time-interpolated daily data Aqua edition (SSF1deg-Day) (Wielicki et al., 1998; Doelling, 2016). The SSF1deg dataset also has auxillariary variables that are computed using the Goddard Earth Observing System (GEOS) model. From this subset of data, surface pressure p_s and U_s variables are derived. AIRS also has a p_s variable which is calculated from a model. The model that AIRS utilizes for p_s calculation is the National Centers for Environmental Prediction Global Forecast System. Comparison of both variables yields very similar results. For the sake of simplicity, CERES~~ daily

1 degree Synoptic product (SYN1deg-Day) (Doelling, 2016, 2017, 2023). This is a combined Terra and Aqua dataset from 2002-2021, and for 2022 it is a combined Terra and NOAA-20 dataset. This CERES dataset combines cloud data from MODIS/GEOS p_s was utilized for the main resultsVIIRS, aerosol data from GEOS, and top of atmosphere radiative flux data from CERES to produce all-sky, clear-sky, and aerosol-free radiative flux profiles.

2.3 GPCP Combined Precipitation Dataset

Precipitation P data for this project was derived from the daily Global Precipitation Climatology Project (GPCP daily) Climate Data Record(CDR), Version 1.3 dataset (Huffman et al., 2001; Adler et al., 2018). GPCP combines satellite observations as well as rain gauge data to produce 1^o daily precipitation amount data.

2.4 CALIPSOMERRA-2 Aerosol Profiles

The CALIPSO satellite dataset utilized is the AL_LID_L3_Tropospheric_APro_AllSky-Standard-V4-20 dataset (Tackett et al., 2018; Wink . CALIPSO was utilized to confirm that the mega-fires are associated with an increase in extinction coefficient EC of aerosols, and which atmospheric layers the largest increases in absorbing aerosols are observed. While all other data sets in this study are daily data, CALIPSO only has monthly data available, and this data is at a much coarser resolution (2^o latitude x 5^o longitude) . Additionally, CALIPSO only has available data between 2006-2021, while all other utilized datasets have data available from 2003-2022 for the relevant seasonal time frame. For level 3 EC data, CALIPSO distinguishes between 3 typesof aerosol: dust, polluted dust, and smoke. This study will primarily utilize the dust and polluted dust EC products. Daily vertical black carbon aerosol mass mixing ratio profiles are derived from the M2I3NVAER data product (Global Modeling And Assimilation Office & Pawson, 2015; Buchard et al., 2015). This product estimates aerosol profiles by assimilating MODIS AOD into the GEOS5 model, which is radiatively coupled to the Goddard Chemistry, Aerosol, Radiation, and Transport (GOCART) aerosol module. The GOCART model includes biomass burning emissions from the NASA Quick Fire Emission Dataset (QFED) version 2.1, which provides daily biomass burning aerosol estimates (Buchard et al., 2015). These profiles were then validated using ground and satellite observations of aerosol profiles. This dataset has been previously used to determine effects of wildfire aerosols in other parts of the world (Raga et al., 2022; Nguyen et al., 2020). The aerosol profiles are archived in a high-resolution hybrid sigma pressure grid, and therefore must be interpolated into 1 degree grid cells, and converted into traditional pressure levels. For the purposes of this paper, only the black carbon variables are analyzed. MERRA-2 separates BC into two types: hydrophobic black carbon BC_{pho} and hydrophilic black carbon BC_{phi}.

2.5 CALIPSO

The Cloud-Aerosol Lidar and Infrared Pathfinder Satellite Observation satellite (CALIPSO) provides observations of aerosol extinction coefficient profiles. MERRA-2 profiles are utilized in the main analysis instead of CALIPSO profiles as CALIPSO data is not temporally consistent with the other datasets utilized in this paper, and because the gridded data is low resolution. More information on CALIPSO can be found in Supplement Section 2.

3 Methods

3.1 Statistics

The bulk of the analysis for this paper involves empirical cumulative distribution functions (CDFs). ~~These CDFs are created by taking a set of data, then fitting a normal distribution . The integral of this normal distribution yields the CDF, which measures the probability of a number, or any number smaller than that number, occurring.~~ Empirical distribution functions are calculated for each variable of interest under differing fire and meteorological conditions, and the shift in each distribution is compared. Plotting two CDFs on the same axis allows for comparison on how likely an anomaly is to be positive or negative under differing circumstances, such as how likely a positive/negative anomaly for a certain variable is to occur during a high (90th percentile) fire dry matter emission ($DM90$) or low (10th percentile) fire dry matter emission ($DM10$) event. The 90th percentile is chosen as the purpose of this paper is to analyze the effects of large fire events on climate, not the effects of fires in general. From the calculated normal distributions, the effect size of one variable's distribution on another variable's distribution are estimated using Cohen's d d. d is an approximation of by how many standard deviations σs the distribution shifts in response to a change in a variable. In this paper, d is calculated to determine the effect size of DM on other variables. d is approximated using

$$d = \frac{\bar{a} - \bar{b}}{0.5\sqrt{\sigma_a^2 + \sigma_b^2}} \quad (1)$$

where $\bar{a}$ is the mean of the ($DM90$) group (group a), and $\bar{b}$ is the mean of the ($DM10$) group (group b), σ_a is the standard deviation of group a, and σ_b is the standard deviation of group b. d=0.2-0.5 is considered to be a weak effect, d=0.5-0.8 is a moderate effect, and d=0.8 or higher is classified as a strong effect.

When comparing two data sets, a two-tailed pooled t-test is used to assess significance, where the null hypothesis of a zero difference is evaluated, with n_1+n_2-2 degrees of freedom, where n_1 and n_2 are the number of elements in each data set respectively. Here, the pooled variance

$$s^2 = \frac{(n_1 - 1)S_1^2 + (n_2 - 1)S_2^2}{n_1 + n_2 - 2} \quad (2)$$

is used, where S_1 and S_2 are the sample variances. For the purposes of this project, the t-test is evaluated at 90$\%$ significance.

3.2 Data Stratification and Comparison

In section 3.1, it was mentioned that CDFs for variable anomalies during anomalously high and low DM emission events are generated to discern to what degree fires impact these anomalies. The purpose of this stratification, particularly stratification of days into anomalously high and low fire events, is to isolate the effects of fires on clouds and/or weather. The remainder of this section will detail how data stratification is accomplished. First, a variable is chosen for analysis (such as CF). Next, this variable as well as the variable(s) that are used to stratify the variable are filtered to include only the region of interest.

As the Aqua satellite does not record data for each gridcell at every time step, wherever a coordinate (latitude,longitude,time) is missing a value for a specific variable, the variable(s) it is being stratified by also has the value at that coordinate replaced by a missing value (and vice-versa). Next, to focus on potential feedbacks fires may have on land, a land-sea mask is applied. Then, the daily regional ~~mean~~ anomaly for each variable is taken. ~~This is done by first averaging over longitude, then taking a weighted average over latitude.~~ Then, the 2003-2022 wildfire seasons are spliced together, which results in a roughly ~~3060 day~~ 3060-day time series. From this 3060 day time series, any days with no data are removed. Next, the average of ~~these time series is removed~~ each day of the wildfire season is removed from each data point in the distribution to give a time series of anomalies for each variable. ~~Then, filters are applied to stratify the variable in question. If the variable is being stratified by one variable (such as DM), the result would be two roughly 306 day long datasets: one stratified by the 90th percentile of the stratification variable, and one stratified by the 10th percentile of the stratification variable. In the cases where the data is stratified by two variables , the result is four datasets. These datasets then have a normal distribution fit to them (Section 3.1) where the average is calculated and a CDF is fit. Once the average is taken for~~ Booleans that filter out days above or below a certain percentile for the stratification variables are then applied simultaneously. For each dataset, ~~σ for each distribution is taken and divided by the square root of the number of data points in each distribution to give the standard error of each dataset~~an empirical CDF is then calculated. Then, the means ~~can be~~ are differentiated from each other to determine if the stratification variable (such as DM) leads to a significant change in the variable anomaly in question. This process can be applied both for a regional average, or on a gridcell-by-gridcell basis. When this process is performed on a gridcell-by-gridcell basis, the Pearson cross correlation coefficient r is determined by spatially correlating the stratified variables with one another. This helps determine if one change in a variable as a result of fires (or other factors) feedbacks onto another to cause a change in anomaly. **Figure 1** serves as a verification of the stratification method, as well as validation of GFED4 emissions data. Monthly cross correlation analysis (Supplement Section 1, **Figure S2**) as well as previous works (Wilmot et al., 2022; Schlosser et al., 2017; Cho et al., 2022) indicate that during large fire events, AOD and/or particulate matter concentration are significantly larger compared to no fire conditions. The significant increase in AOD over most of the southwestern US supports the assertion that GFED4 fire emissions are an acceptable indicator of large fire occurrences.

3.3 Regions of Interest

First, the region within the southwestern US in which the most significant fire emissions originate ~~from~~ was discerned. Based on what is generally considered to be the time of year in which most wildfires occur in the western US (Urbanski, 2013; Urbanski et al., 2011), data was collected from June 1st-October 31st for the 2003-2022 time ~~frame~~period. 2003-2022 was chosen as this is the time ~~frame~~ period in which Aqua satellite data is available for the fire season. Analysis was limited to fire seasons as opposed to the entire year so that the threshold for what constitutes a 90th percentile fire is increased. First, for each gridcell, the 2003-2022 seasonal average daily DM emissions was taken. The portion of the southwestern US that had the largest 2003-2022 seasonal average daily DM emissions is the region that shall be referred to as "northern California" (nCA), which is highlighted in the blue box in **Figure 1a**. The reason for limiting DM data to this region is again to ensure that the threshold for 90th percentile DM is kept high. The nCA region is characterized by temperate forests along the coastline, in the far north, as well as the east. Agricultural lands are scattered throughout just about every gridcell in nCA, with higher concentrations in the central valley as well as the coastal north. Grasslands are also found throughout most gridcells grid cells in this region, with higher concentrations in central CA. The dominant contributor of DM in this region is the temperate forests in the north (**Figure S1S3**). At this time of year, predominant wind patterns in nCA would favor transportation of smoke from these fires to northern Nevada. During the fire season, northwesterlies tend to blow across nCA towards northern Nevada, and south westerlies blow through the central valley and Sierra Nevada range (Zaremba & Carroll, 1999; LeNoir et al., 1999). Therefore, the expectation is for the majority of wildfire aerosols to be concentrated in nCA, and neighboring northern/central Nevada. In differentiating AOD anomalies on high nCA DM on high fire days and DM days and AOD anomalies on low nCA DM on low fire days, AOD is found to be significantly higher anomalously positive in both nCA and Nevada (**Figure 1b**), confirming this suspicion. Therefore, from hypothesis. However, there are also significant AOD anomalies throughout the entire region. For reasons that will be explained in **Section 4.1**, the main analysis will still be relegated to northern CA and Nevada. From this point forward, the focus will be on the effects of the fires in the blue box in **Figure 1a** (nCA) on the area highlighted in the green box (nCA-NV) in **Figure 1b**.

3.4 Heating Rate

Aerosol shortwave heating rate of the atmosphere SWH_{aer} was calculated using

$$\frac{\partial T}{\partial t} = SWH_{aer} = \frac{g}{c_p} \cdot \frac{\Delta F_{aer}}{\Delta p} \quad (3)$$

Figure 1 also serves as a verification of the stratification method, as well as validation of GFED emissions data. Monthly cross correlation analysis (Supplement Section 1) as well as previous works (Wilmot et al., 2022; Schlosser et al., 2017; Cho et al., 2022) indicate that during large fire events, AOD where t is time in days, g is gravity, c_p is the heat capacity at constant pressure, F_{aer} is the shortwave radiative effect of the aerosols, and /or particulate matter concentration are significantly larger compared to no fire conditions. The significant increase in AOD over most of the southwestern US supports the assertion that GFED fire emissions are an acceptable indicator of large fire occurrence. p is pressure. F_{aer} itself was derived from the CERES SYN1deg-Day downward and upward shortwave radiative fluxes. F_{aer} between two atmospheric layers is given by

$$F_{aer} = SWd_1 - SWu_1 - (SWd_2 - SWu_2) \quad (4)$$

where SWd_1 denotes downward shortwave flux at the higher layer, SWu_1 denotes upward shortwave flux at the higher layer, SWd_2 denotes downward shortwave flux at the lower layer, and SWu_2 denotes upward shortwave flux at the lower layer.

3.5 CALIPSO

To determine the difference in EC profile between anomalously high and low fire events, the average for each aerosol type's EC at each pressurelevel was taken over ($DM90$) months and ($DM10$) months in the 2006-2021 range (the time frame in which CALIPSO data is available) in the region of interest. The difference between these two profiles is then taken.

The motivation for this process is for one, to remove the effects of potential background aerosols such as BC or OA (from anthropogenic sources such as fossil fuel burning) and isolate the effects of the aerosols emitted from mega-fires. The resulting profile then depicts the effects on the vertical EC profile that fires have. The EC profile of the aerosols is not further stratified as the CALIPSO data is monthly.

4 Results

4.1 Vertical Distribution of Absorbing Aerosols in nCA-NV RegionHigh & Low Surface Relative Humidity Stratification

The three absorbing aerosols that are associated with fires that can be discerned by CALIPSO are smoke, dust, and polluted dust. While dust is not emitted from biomass burning, a number of studies have linked fires to concurrent dust emission through creation of powerful convective updrafts (Wagner et al., 2018, 2021) and delayed dust emissions through wildfire clearing of vegetation (Wagenbrenner et al., 2013, 2017; Yu & Ginoux, 2022). Past observations and modelling experiments have shown dust to create fingerprints of a traditionally-defined semi-direct effects (Tsikerdekis et al., 2019; Amiri-Farahani et al., 2017; Helmert et al., . effect where aerosols coincide with clouds would entail an anomalous warming of the cloud layer, and a corresponding decrease in RH. However, increases in non-polluted dust during fires may be related to the concurrence of high winds that tend to be a driver of the mega-fires themselves. Emissions of polluted dust, however, are far more likely to be related to fires, as this aerosol species is a combination of dust and smokey aerosolsthe meteorological conditions around which fires tend to occur need to be considered. As previously stated, large fires tend to occur during fire weather, which includes hot, dry, and windy conditions (Varga et al., 2022). Hot and dry conditions themselves are associated with high pressure anomalies in this region (**Figure S4**). Therefore, these fire weather conditions need to be "filtered out" to determine any potential semi-direct effects. Therefore, focus was placed upon smoke and polluted dust. Polluted dust is a mixture of smoke and dust, and therefore should have stronger SW absorption than dust alone. **Figures 2a** & **2b** depict monthly 2006-2021 nCA-NV regional average $EC(DM90)$ -$EC(DM10)$ in the daytime (**Figure 2a**) and the nighttime (**Figure 2b**) for both smoke and polluted dust. These plots demonstrate that polluted dust and smoke EC increases significantly in most parts of the troposphere in months where an anomalously large fire occurs. This includes altitudes with pressures p less than 500hPa, where there are relatively large and significant increases in polluted dust (**Figures 2c, 2d**). These high altitude changes are important as in $(DM10)$ months, there is no smoke or polluted dust EC above roughly p =400hPa (**Figure S3,S4**) , which supports the assertion that wildfire aerosol plumes deposit absorbing aerosols high in the troposphere. However, it should be noted that there are a few altitudes where there is anomalously low smoke EC observed, such as around p =900hPa in the daytime profile and around 500-400hPa in the nighttime profile. The standard errors on these negative differences are quite high however, and may be dominated by an outlier month with abnormally high smoke concentration in the $(DM10)$ emission months (possibly from transportation of smoke from a fire outside of the region of interest).

4.2 ~~High & Low Pressure Extremes Stratification~~

~~The fingerprints of a semi-direct effect would entail an anomalous warming of the cloud layer, and a corresponding decrease in RH. However, the meteorological conditions around which fires tend to occur need to be taken into account.~~ ~~**Figure 3** depicts cumulative distribution functions (CDFs) for meteorological conditions under high p_s~~ in addition to DM, variables need to be stratified by a second variable to account for the influence of meteorology on P, CF, and cloud properties. Fire season data was stratified by high (75th percentile) vs low (25th percentile) T_s, RH_s, U_s, and surface pressure to determine which variable was associated with the largest DM, and successfully filtered out fire weather condition anomalies. The 75th/25th percentiles were chosen for the potential second stratification variables as opposed to extremes (90th/10th percentiles) to ensure a robust number of data points, and to have a dataset that is more representative of common conditions in the region. **Figure 2** depicts CDFs for meteorological conditions and DM under high RH_s extremes (~~p_s90) and low p_s~~ RH_s75) and low RH_s extremes (~~p_s10) . High p_s~~ RH_s25) in the entire southwestern US. RH_s was chosen as the second stratification variable, as stratifying nCA DM by high (RH_s75) and low RH_s conditions (RH_s25) and differentiating the means of these distributions yields a significant DM anomaly of $\Delta DM = -1.04\text{e-}4 \pm 3.5\text{e-}5$ kg m^{-2} day^{-1}. The absolute value of this anomaly is an order of magnitude higher than the differences in mean DM between high and low conditions of the other potential stratification variables (surface pressure, T_s, and U_s) (**Figure S4, Figure S5, and Figure S6**). This indicates that fire occurrence/fire emission are more dependent on RH_s than these other fire weather variables. Low RH_s extremes in the southwestern US are associated with significantly higher T throughout the troposphere/surface, significantly reduced RH throughout the troposphere/surface, and ~~reduced~~ significantly lower CF, while ~~low p_s~~ high RH_s extremes are associated with the opposite (**Figure ~~3~~2**). This demonstrates a need to separate the effects of fires from the meteorological effects of ~~high p_s~~ low RH_s extremes, as positive DM anomalies are significantly more likely to occur on (~~p_s90~~RH_s25) days as opposed to (~~p_s10) days. Additionally, **Figure 3h** demonstrates that surface wind speeds tend to be larger in the nCA-NV region during p_s10 days. This could impact the transportation of the BB/polluted dust aerosols, potentially allowing for further transportation. **Figure 4a** demonstrates that AOD is not significantly different whether fires occur during (p_s90) or (p_s10) days. However, **Figure 4b,c** demonstrate that the distribution of AOD is significantly different between the positive/negative p_s extremes. Under (p_s90) conditions, the area with the highest AOD is the origin of the BB aerosols: nCA. Under (p_s10) conditions, the AOD is significantly high over both nCA and Nevada.~~

4.2 ~~Responses in Temperature & Humidity Profiles~~

RH_s75) days, as which is expected as moisture, and moist plants, suppress the ability of fires to grow and be maintained (Minnich & Chou, 1997; Ford & Johnson, 2006). The immediate direct effect of BB aerosols tends to be a net cooling of the surface (Sakaeda et al., 2011; Abel et al., 2005). However, certain semi-direct effects, such as the burning off of low clouds, may overpower this effect, leading to a net surface warming. As the meteorological conditions associated with ~~high pressure~~ low RH_s days are also hallmarks of a semi-direct effect (**Figure ~~3~~2**), from here onward data will be stratified into four categories: one with high DM and high ~~p_s~~ RH_s (DM90,~~p_s90~~RH_s75), one with low DM and high ~~p_s~~ RH_s (DM10,~~p_s90~~RH_s75), one with high DM and low ~~p_s~~ RH_s ($DM90$,~~p_s10~~RH_s25), and one with one with low DM and low ~~p_s~~ RH_s ($DM10$,~~p_s10~~RH_s25). In differentiating the average of the variables on ($DM90$,~~p_s90~~RH_s75) days and ($DM10$,~~p_s90~~RH_s75) days, the effects of fires can be discerned independent of the meteorological conditions that come with high ~~p_s~~ DM extremes. Additionally, ~~in~~ comparing the ($DM90$,~~p_s10~~RH_s25) dataset to the ($DM10$,~~p_s10) dataset, the effects of high p_s are not present, so this further isolates the effects of the fires.~~ RH_s25) potentially allows the effect of fires to be discerned during fire weather, as the meteorological conditions in both distributions should not be significantly different from one another. **Figure 3** demonstrates that the effect of fires on AOD under both high and low RH_s stratifications is significantly positive anomalies in the nCA-NV region. The increase in mean AOD is larger under low RH_s at 0.24 $\pm$ 0.04. The corresponding change under high RH_s is 0.13 $\pm$ 0.05. As the AOD is consistently significant only in the nCA-NV region under both stratifiactions, this region will be the focus of the study.

4.2 Vertical Distribution of Black Carbon and Absorption in nCA-NV Region

Freshly emitted BC is highly hydrophobic, and as it ages it becomes less resistant to accumulating water droplets (Lohmann et al., 2020) . BC has an average lifetime of 1 week (Lohmann et al., 2020), and the aging process begins after 1-2 days (He et al., 2016) . Furthermore, in a region with such low fire season wet deposition such as the southwest US, the BC on average can live much longer than one week (Ogren & Charlson, 1983). Therefore, hydrophobic and hydrophilic BC profiles are important to differentiate because they can give an idea of how long the BC stays in the atmosphere, and it hints at how much BC can contribute to indirect and semi-direct effects. **Figure 4** displays high compared to low DM mass mixing ratio anomalies for BC_{phi}, BC_{pho}, and combined BC on high and low RH_s days. Significant positive anomalies of BC mass mixing ratio are present from 950Pa-300 hPa for all types of BC under both $(DM90, RH_s75)$ and $(DM90, RH_s25)$ conditions compared to the corresponding low fire conditions. The most significant increase in BC is from about 950-600 hPa for the $(DM90, RH_s75)$ days, and from 950-550 hPa for the $(DM90, RH_s25)$ days. Comparing the MERRA-2 BC profiles to the CALIPSO $DM90$-$DM10$ months 2006-2021 smoke aerosol daytime and nighttime extinction coefficient profile, MERRA-2 places more absorbing aerosol below 700 hPa, while CALIPSO generally places more absorbing aerosol above 700 hPa (**Figure S7**). Therefore, it is important to note that CALIPSO profiles do not agree with MERRA-2 when it comes to the positioning of the smoke in the troposphere. However, as the MERRA-2 and CALIPSO profiles are not temporally consistent, the comparison between these profiles is not 1-1. Additionally, as the CALIPSO profiles are not temporally consistent with the rest of the data in this paper, their use is not preferred over the MERRA-2 profiles.

There is roughly an equal amount of BC_{phi} and BC_{pho} during both high and low RH_s days, indicating that on these days there is roughly as much fresh and aged aerosol in the troposphere. This is important as the quantity of BC_{pho} indicates that microphysical effects are possible as it suggests a large amount of CCN are present in the troposphere. Additionally, the presence of aged BC indicates that the BC can affect the atmosphere radiatively over the course of multiple days. To estimate the impact of these aerosols on the troposphere over time, a SWH_{aer} profile was created from CERES radiative flux data (**Figure 5**). Shortwave profiles used to generate these heating rate profiles, along with LW profiles, can be found in **Figure S8**.

Under both $(DM90, RH_s75)$ (**Figure 5a**) and $(DM90, RH_s25)$ (**Figure 5b**) RH_s conditions compared to the corresponding low DM conditions, there is a positive SWH_{aer} anomaly from 850 hPa to the next highest pressure level in the CERES dataset, 500 hPa. For high RH_s, this corresponds to a heating rate of $SWH_{aer} = 0.041 \pm 0.016$ K day^{-1}, and for low RH_s this corresponds to a heating rate of $SWH_{aer} = 0.093 \pm 0.019$ K day^{-1}. A highly idealized prior modelling study on the shortwave absorbing properties BC globally found that a heating rate of about 0.8 K day^{-1} from increasing BC tenfold was associated with around 0.8 K of warming (Stjern et al., 2017). Assuming linearity, the 0.04-0.09 K day^{-1} heating rate observed in **Figure 5** would therefore correspond to around a 0.4-0.9 K temperature anomaly. Spatially, the 850 hPa-500 hPa heating rate is significant over almost all grid cells in the region of interest where there is data, with the most positive heating rates over eastern nCA and eastern Nevada (**Figure S9**).

4.3 Responses in Temperature, Humidity, & Cloud Profiles

Figure 6 displays 2003-2022 June-October nCA-NV vertical profiles of high minus low fire days' vertical profiles of the fire effect on T (**Figure 5a,d** and RH (Figure 5c,f)profiles. **Figure 5a-c** **Figure 6a,e**), and RH (**Figure 6c,g**) profiles. **Figure 6a-d** are stratified by high p_s, while **Figure 5d-f** are stratified by low p_s. These profiles demonstrate that when anomalously large fires are occurring, whether it is during high or low pressure extremes, temperature is significantly anomalously high at all points of the troposphere at $p \geq$250hPa compared to conditions with anomalously low firesRH_s, while **Figure 6e-h** are stratified by low RH_s. In both **Figure 5a6a** and **Figure 5d6e**, the temperatures in the 850hPa to 250hPa temperature anomalies in the 850 hPa to 300 hPa pressure level range are consistently significantly higher than the surface layer (900hPa to 1000hPa). Comparing significant and positive at around 1 K. Since the aerosol heating rate accounts for approximately 0.4-0.9 K of warming, the semi-direct effect of these aerosols accounts for about 40-90% of this anomaly. Comparing **Figure 56** to **Figure 24**, the positive differences in temperature anomaly are generally consistent with the positive differences in polluted dust and/or smoke EC. In comparing BC anomalies. Under both high RH_s (**Figure 5d6c**to) and low RH_s (**Figure 5e6g**) conditions, RH anomalies in the 700hPa to 250hPa range (and at sea level) are significantly lower when anomalously large fires occur during low pressure extremes. throughout the entire profiles are negative but are only consistently significant during high RH_s extremes. The AIRS CF profile under high RH_s conditions (**Figure 6d**) demonstrates significant negative anomalies from 300 hPa-600 hPa that are consistent with significant negative RH anomalies and significant positive T anomalies. However, there is an increase in CF at 850 hPa (**Figure 6d**). This pressure level corresponds to the highest concentration of BC_{phi} (**Figure 4c**), and perhaps this indicates at this pressure level there is cloud seeding occurring. For the low RH_s profile, there is only a significant negative cloud anomaly close to the surface at 925 hPa (**Figure 6h**).

Aside from temperature, the other potential factor that could affect RH is that of specific humidity, which is analogous to water mass mixing ratio M_{H_2O}. Utilizing the same process that generated the T and RH profiles, profiles of **Figures 6b,f** depicts the effect of fires on M_{H_2O} were generated for high and low p_s extremes (**Figures 5b,e**)anomalies under high RH_s and low RH_s conditions respectively. There is no significant anomaly under high p_s conditions , but under low p_s there are significant negative anomalies at 1000hPa, and 500-300hPa. This means that the negative or low RH_s conditions but is consistently positive at 700 hPa and below. Furthermore, the changes in the RH anomaly in the high troposphere under high fire conditions is due at least in part to a negative specific humidity anomaly. **Figure 6** depicts high minus low DM extremes' 500hPa-250hPa and 700hPa-500hPa profile follow the changes in the T profile as opposed to the M_{H_2O} profile, implying the positive T anomalies generally dominate the change in RH anomalies.

While these profiles provide a general overview of how T, M_{H_2O}, and RH anomalies during low p_s extremes. In both the , and CF are changing over the region of interest, it is important to determine if these changes are consistent spatially with one another, as well as whether the changes coincide with BC anomalies. As the T, RH, and CF anomalies are strongest during high and low/mid-troposphere in the nCA-NV region (highlighted in the green box) RH_s days, the focus from here will be on the meteorological effects of high DM on high RH_s days. **Figures 7-11** depict the effect of fires on the spatial distributions of BC, there are significant increases in T, M_{H_2O}, RH, and CF anomalies at each AIRS pressure level up to 200 hPa on under high RH_s conditions. The positive MERRA-2 BC anomalies in **Figure 7** correlate positively and significantly with MODIS AOD for each pressure level between 925 hPa-300 hPa (**Figures 7b-h**), and are spatially consistent with positive AIRS T anomalies (**Figure 8**). Shifting attention to **Figure 9**, there appear to be significant negative anomalies in M_{H_2O} in northeastern Nevada from 700 hPa-400 hPa, and significant positive anomalies over grid cells associated with large fires (**Figure 1a**) in the lower troposphere (925 hPa-850 hPa). Comparing these changes in T and decreases in M_{H_2O} spatially to changes in RH . However, in the high troposphere, there is a significant decrease (**Figure 10**), it appears that changes in T tend to dominate changes in RH over CA, western NV, and southern NV while changes in M_{H_2O} over Nevada that is not present in appear to contribute to the negative RH anomaly in northeastern NV. Additionally, the low/mid troposphere. Therefore, decreases in positive M_{H_2O} at 850 hPa appears to mitigate the negative RH anomalies at the same level, which may explain why BC appears to be able to act as a CCN at this level but not others: RH does not decrease enough to prevent clouds from forming. The increase in the high troposphere are likely in part due to changes in M_{H_2O} in addition to increases in has a myriad of possible explanations. It may be due to emission of moisture from the burned vegetation (Jacobson, 2014; Dickinson et al., 2021), from lofting of water vapor from the surface to higher levels of the atmosphere (Yu et al., 2024), or from moisture advection due to a change in wind vectors from the northeastern part of Nevada towards CA (**Figure S10**). Viewing **Figure 11c**, the increase in CF at 850 hPa appears to be driven predominantly by a few significant and large coastal CF anomalies. This indicates that there is an increase in shallow marine clouds at this pressure level, while clouds at other pressure levels are generally being suppressed. **Figure 11** demonstrates that significant negative CF anomalies are generally spatially consistent with negative RH anomalies from 700-400 hPa. The significant negative CF anomalies in northeastern Nevada that correspond with significant negative RH anomalies, but not significant positive T anomalies, at 700 hPa and higher indicate that the difference in clouds in this region is specific humidity dependent. This may be due to a transport of moisture outside of these grid cells due to anomalously positive southeastern wind speed anomalies in some of these grid cells (**Figure S10b**) that advect moisture towards southern California and southern Nevada, however further scrutiny is warranted to confirm this. It is unknown if the fires are the cause of this difference in specific humidity anomaly, but this is further explored in not known if these wind speed anomalies are related to warming from the BB aerosols, or if these wind speed anomalies in this region are an artifact. Changes in wind vectors are further analyzed in supplement section 2 of the supplement . 3. As the change in T is the more robust signal over all parts of the troposphere, the changes in T will be the focus of the remainder of the paper.

4.4 Changes in Cloud FractionType, Precipitation, and Shortwave Flux

Figure 5 implies that during anomalously large fire events, there is a significant increase in temperatures in the low, mid, and high troposphere compared to anomalously low fire conditions. Does this increase in temperature translate to a decrease in With AIRS data indicating that large fires are associated with enhanced T, as well as lower RH and CF, and therefore a change in the radiative balance? it is essential to determine how liquid vs ice clouds are impacted, and what the corresponding impacts on P and radiative balance are. **Figure 712** displays CDFs for nCA-NV regional average variable anomalies during high DM/low p_s RH_s days (solid red), low DM/high p_s RH_s days (dashed red), high DM/low p_s RH_s days (solid blue), and low DM/low p_s RH_s days (dashed blue). **Figure 7a12a** and **Figure 7b12b** demonstrate that during both high and low p_s high RH_s extreme days, the mean effect of fires on the liquid water cloud fraction CF_{lw} anomaly distribution and cirrus cloud fraction anomaly CF_{cir} anomaly are shifted significantly leftward under high DM conditions. This implies that when anomalously large fires occur, there is a significantly higher probability (at the 90% confidence interval) of seeing a negative distribution is a significant shift towards a preference for negative anomalies. The effect of the large fires creates an average -0.04 ± 0.02 CF_{lw} and/or anomaly, and an average -0.05 ± 0.04 CF_{cir} anomaly . While the distribution of all other variables depicted in **Figure 7**, such as under high RH_s conditions. In addition, MODIS total CF , cloud top height CTH, P, and outgoing top of atmosphere shortwave flux $TOA\ SW$ flux, are shifted leftward on high DM days compared to low DM days, the shifts are not significant during high p_s extremesshifts by -0.07 ± 0.05 under the same stratifications. Precipitation also shifts significantly by -0.3 ± 0.23 mm day^{-1}. However, these shifts are significant for low p_s only for high RH_s extreme days (**Figure 712**). The explanation for as to why the distribution shifts farther leftward towards negative anomalies when anomalously large fires occur during low pressure compared to high pressure high RH_s compared to low RH_s extremes lies in **Figure 52**. High pressure extremes create conditions favorable for sinking air. During high pressure extremesDuring low RH_s days, RH throughout the troposphere is already significantly lower than normal conditions (**Figure 2e**), as temperatures throughout the troposphere are already high (**Figure 2c**) and atmospheric water vapor content is low. This creates conditions of cloud-free skiesnegative CF anomalies (**Figure 2f**). Therefore, further decreasing the already low RH increasing the already high T should not lead to significantly lower cloud fraction , P, or outgoing $TOA\ SW$ flux as CF as RH is already low., and clouds require 100% RH to form. This can also be explained by the RH profile in **Figure 6g**, which demonstrates through most parts of the troposphere that RH is not significantly lowered due to fire effects. However, during low DM/low p_s days, high RH_s days, **Figure 712** demonstrates that conditions are favorable for clouds and rain. This is because during these low pressure high RH_s extremes, T is lower and RH is high. Therefore, when anomalously large fires introduce aerosols that create a semi-direct effecta positive T anomaly, the drop in RH is significant enough to reduce the chances of seeing positive cloud/rain precipitation anomalies. In response to the higher probability of negative cloud fraction anomaly, the probability that SW radiation will be reflected back into space decreases. The effect sizes of high DM emissions on nCA-NV regional averages of the variables in This reduction in top of atmosphere shortwave flux leads to a net increase in cloud only (all-sky minus clear-sky) top of atmosphere radiative forcing TOA_{cld} (**Figure 712f**are depicted in **Figure 8**. **Figure 8a** demonstrates that during high p_s extremes, anomalously large fires have a weak-to-no effect size on the relevant variables. For low p_s extremes, the anomalously large fires have a moderate-to-strong effect size on the relevant variables.

Thus far, the focus of this project has been on the regional average of the nCA-NV region. However). Though it should be noted that this increase is not significant, it is essential to determine if the changes in the relevant variables are spatially consistent. As the fire semi-direct effect signal is strongest during significant low pressure days, the focus from here will be on the meteorological effects of fires during high DM/low p_s days. significant and positive over much of the region marked by a decrease in CF (**Figure 13e,h**), with a significant spatial cross correlation of $r = -0.67$. Regional all-sky SW and LW responses can be found in **Figure 9S11**.

Figure 13 displays composite differences between meteorological variables on high DM/low p_s high RH_s and low DM/low p_s days ' meteorological variables highRH_s days for each gridcell over the entire southwestern US. **Figures 6a13a,b** display the composite differences in cloud layer (700hPa850 hPa$\geq p \geq$250hPa300 hPa) temperature T_{CL} and cloud layer relative humidity RH_{CL}. These plots depict that T_{CL} significantly (significant changes are marked with a black dot in each gridcell) increases almost everywhere across California and Nevada, with the most significant increase in the green box (the nCA-NV region). The differences in T_{CL} correlate significantly with differences in AOD (DM90,p_s10)-AOD(DM10,p_s10) at $r = 0.79$ at $r = 0.70$ across the entire southwest. The decreases in RH_{CL} have a very similar spatial distribution to T_{CL}, with the strongest decreases in the nCA-NV region. Again, this correlates significantly with AOD with $r = -0.77$ $r = -0.60$ over the entire southwest. While the increases in cloud layer T are widespread across all of California and Nevada, significant increases in T_s (**Figure 9c**), decreases in RH_s (**Figure 9d**), decreases in CF (**Figure 9e**), decreases in CTH (**Figure 9f**), decreases in P (**Figure 9g**), and decreases in TOA SW flux (**Figure 9h**) are essentially exclusive to the nCA-NV region. The differences in all of these variables across the southwestern US correlate significantly with AOD, supporting the assertion that aerosols concurrent with fires create are associated with semi-direct effects. Of particular note are the changes in T_s and P, which are two variables intrinsically related to fire duration. A spatial cross correlation of the change in T_s and TOA SW yields r =-0.59, which is significant at the 90% confidence interval. Furthermore, Spatially correlating P with RH_{CL} using the same method yields an even stronger correlation of r =0.80. Breaking down the changes in yields a significant correlation of $r = 0.44$, implying that the reduction in P is related to the semi-direct effect. However, it should be noted that though the regional P anomaly is significant and negative, that it appears to be dominated by just strong changes in just a few gridcells. T_s correlates significantly with AOD over the southwestern US, with $r = 0.51$, and is generally spatially concurrent with increases in T_{cl} with $r = 0.72$. The equivalent for **Figure 13** for low RH_s days is given in **Figure S12**. Of note for this supplementary figure is that there are weak, but significant and widespread, negative CFinto liquid and ice cloud components, it appears that cirrus clouds contribute the most to the decrease in CF and CTH. **Figure 10** depicts composite differences between high , RH, and P anomalies over nCA and eastern Nevada, despite not being significant in the regional average (**Figure 12c,e**). This implies that the effects of the absorbing aerosols seen during high RH_s days are also prevalent on low RH_s days, but weaker and less widespread due to the lower availability of moisture.

While cross correlations indicate that there is a statistically significant relationship between fires and meteorology, practical significance needs to be established as well. The effect sizes of high DM ~~/low p_s and low DM/low p_s days' CF_{lw}~~ emissions on nCA-NV regional averages of the variables in **Figure 12** and ~~CF_{cir}. The differences in CF_{lw} are spatially consistent with the changes in RH in the 700-500hPa levels of the troposphere, while The differences in CF_{cir} are spatially consistent with the changes in RH in the 500-200hPa levels of the troposphere (**Figure 6**).~~ **Figure 13** are depicted in **Figure 14**. For high RH_s extremes (**Figure 14a**), the anomalously large fires have a moderate-to-strong effect size on most of the relevant variables. **Figure 14b** demonstrates that during low RH_s extremes, anomalously large fires have a weak-to-no effect size on the relevant variables, aside from T_{cl} in which fires have a very strong effect size on.

4.5 Cloud Microphysical Effects

Up to this point, we have investigated aerosol direct/semi-direct effects on clouds. Aerosols may also influence clouds via microphysical effects, which are investigated in this section. High fire emissions under ~~both low and high p_s~~ high RH_s conditions are associated with non-significant differences in ~~liquid and ice R_{eff} (~~microphysical variables (**Figure ~~11~~15**). ~~Under high fire /high p_s extremes, there~~ Spatial maps of the fire effect on R_{eff} and LWP under high RH_s conditions show a mix of areas with positive and negative changes, most of which are not significant (**Figure S13**). Although there is a small tendency for negative R_{eff} anomalies to occur in Nevada and a small tendency for negative LWP anomalies to occur in nCA and western NV. Since negative R_{eff} anomalies can affect precipitation, the spatial distribution of R_{eff} anomalies (**Figure S13, Figure S14**) was compared to the spatial distribution of P anomalies (**Figure 13, Figure S12**) under high compared to low DM conditions. Significant negative R_{eff} anomalies were not found to be spatially consistent with significant negative P anomalies under either high or low RH_s conditions. This casts doubt on wildfires in this region creating microphysical suppression of P.

There are significant regional changes in liquid R_{eff} and LWP under low RH_s conditions (**Figure 15, Figure S14**). Liquid R_{eff} significantly increases under these conditions, which is contrary to what one would expect as a response to increased AOD (Twohy et al., 2021; Conrick et al., 2021; Fan et al., 2016). One possible explanation for this increase in R_{eff} is that R_{eff} is directly proportional to temperature (Martins et al., 2011), and perhaps the effects of the T anomaly dominate over the condensation of new droplets onto BC_{phi}. Alternatively, this increase may be driven by changes in atmospheric dynamics, as increased updraft strength and enhanced turbulence could lead to increased coalescence (Khain, 2009). Coincident with the strongest increase in R_{eff} (at the northernmost coast of California) under these conditions is ~~an increase in ice water path IWP. IWP scales positively with T, so this is~~ a ~~fingerprint of a dominate radiative effect (Ou & Liou, 1995). Furthermore, there is a~~ significant ~~decrease in LWP under anomalously high fire/low p_s conditions~~ negative (upward) pressure velocity anomaly from 1000 hPa-925 hPa, which implies that an increase in upward convection near the surface may be a factor of the increase in R_{eff}, as an upward pressure velocity should increase droplet lifetime (**Figure S15**). It is also noted that there are negative pressure velocity anomalies under high RH_s conditions from 1000 hPa-850 hPa (**Figure S16**), and this corresponds with an increase in R_{eff} near the Bay Area.

The fire effect on LWP under low RH_S conditions is significant a decrease (**Figure 15c**). This significant ~~decrease in~~ negative LWP anomaly may be due to the ~~decrease in RH, which reduces~~ negative RH_{cl} anomaly (**Figure S12b**), as lower saturation of the air would reduce liquid water within clouds. This decrease in LWP may be of importance, as LWP scales positively with cloud albedo (Han et al., 1998). Therefore, this decrease in LWP may contribute to an increase in absorbed solar radiation at the surface. In summary, while the nCA fires significantly inject ~~of~~ aerosols into the troposphere, these aerosols do not appear to generally act as CCN, and instead ~~burn~~ contribute to a positive T anomaly that burns off clouds. ~~Previously, BC has been shown to aid cloud droplet/ice formation, but only after the particles have undergone over a week of aging (Lohmann et al., 2020). Therefore, the freshly emitted BC during the anomalously high fire events may be too hydrophobic to act as CCN~~This may be because BC is generally more hydrophobic compared to other aerosols, and instead the radiative effects of the aerosol dominate. ~~Additionally, the warming effects of these aerosols may reduce RH to the point where clouds are unable to form in the first place.~~

5 Discussion

The results of this paper indicate that large fires in nCA are concurrent with significant amounts of absorbing aerosols and a warmer troposphere. When the fires occur during ~~low p_s extremes~~high RH_s conditions, this increase in T (**Figure 8, Figure 13a**) is associated with a significant decrease in RH in the low, mid, and high cloud layers (~~700hPa-250hPa~~850 hPa-300 hPa) at the 90% confidence interval (**Figure 10, Figure b**). This decrease in RH is associated with a reduction of clouds, which results in a reduction in CF and P significantly in the nCA-NV region. This reduction in clouds is then associated with ~~a reduction in outgoing TOA SW flux. This reduction in outgoing TOA SW flux is concurrent with~~ an increase in ~~T_s and a reduction in RH_s in the nCA-NV region. However, this warming effect may be somewhat muted by a reduction in~~ TOA radiative flux (**Figure 13h**), despite a decrease in CTH ~~, which could increase outgoing TOA LW flux , presumably as a result of a disproportionate reduction in CF_{cir} compared to CF_{lw} seen in~~ (**Figure** ~~**9**~~**13f**). In short, during ~~low pressure~~ high RH_s extremes, fires in nCA appear to create a positive feedback that entails emissions of absorbing aerosols that warm the troposphere, creating a semi-direct effect. This semi-direct effect ~~then creates~~ contributes at least partially to conditions more favorable to fires~~, including warmer surface temperatures and reduced P, as a result of reduced cloud cover and cloud layer RH~~. Significant reductions in nCA P may prolong the wildfire season further into autumn (Goss et al., 2020), and increases in ~~T_s~~ T as well as decreases in ~~RH_s~~ RH may create conditions more favorable for more fires to ignite and grow ~~. This positive feedback may~~ (Varga et al., 2022). Under the low RH_s stratification, regional warming of the cloud layer and surface becomes larger, more widespread, and less uncertain (**Figure 6e, Figure S12**). This is likely due to a significantly higher amount of AOD/BC present in the atmosphere on these days (**Figure 3, Figure 4**), which corresponds with a stronger heating rate (**Figure 5b**). However, with a higher likelihood of lower RH_{cl} anomalies during low RH_s conditions (**Figure 2e**), the result is a muted, but significant, CF and P suppression that is limited to only nCA.

The results of this paper are consistent with the findings of Thornhill et al. (2018), who utilize a similar methodology to this paper to analyze the effects of large fires. They ran the Met Office Unified Model using aircraft observations of AOD and BB aerosol properties. They compared meteorological variables in high vs low fire emission conditions over South America and found a clear sky shortwave heating rate of the low-to-mid troposphere that is larger (0.2 K day^{-1}), but comparable, to the heating rates calculated in this paper. They found that their heating rate was associated with a stronger semi-direct effect than the one observed in this paper, with CF decreasing throughout all the troposphere, which would be consistent with their stronger heating rate. Though not related to fire, an aircraft observational study of anthropogenic BC over the Bay of Bengal found a BC heating rate of around 0.5 Kday^{-1} (Kant et al., 2023), which demonstrates that either the biomass burning aerosols in this study are associated with a weaker heating rate, or that the shortwave absorption estimated by CERES is underestimated. The heating rate calculated in this paper is consistent with the calculated heating rate of a modeling study that simulate a global 10$\times$ BC scenario, which demonstrate a 0.08 Kday^{-1} (Stjern et al., 2017), a number consistent with the heating rate over the region of interest. Furthermore, the results of this study are consistent with numerous other satellite observational studies over the tropics and subtropics that demonstrate that aerosols associated with wildfires can burn off clouds when at a coincident height, resulting in a positive radiative forcing (Wilcox, 2012; Kaufman et al., 2005; Ackerman et al., 2000; Hansen et al., 1997). Additionally, the reduction in CF and P is consistent with the results of Chen et al. (2014), which was a biomass burning aerosol modelling experiment conducted over the United States. However, their proposed mechanism for these decreases was a change in convection. Concerning the increase in M_{H_2O} above sites of fire emission in **Figure 9b,c**, this is consistent with a recent study that found comparable results (Yu et al., 2024), however they found more water vapor higher in the troposphere than this paper. Additionally, it is noted that the observed microphysical effects of the BB aerosols in this paper, namely the lack of a regional decrease in R_{eff}, contrast to another observational study that overlaps with the region of interest in this paper (Twohy et al., 2021). An important note about that study, however, is that it only sampled the 2018 wildfire season while this study focuses on the entire 2003-2022 time span. Finally, one last caveat to this study is that while it has been demonstrated that the T anomalies in **Figure 6, Figure 7, and Figure 8** are associated with biomass burning aerosols during large fire events, this does not imply that the aerosol semi-direct effect is the only contributor to the observed meteorological anomalies. As previously stated, at most 40-90 % of the T anomaly is accounted for by the semi-direct effect. One possible source of noise is wind. **Figure S10** depicts a positive wind speed in northern Nevada that may be influencing cloud cover over that part of the region, and it is unknown if this signal has anything to do with the semi-direct effect. Additionally, wildfires are associated with an increase in sensible heat flux from the combustion of biofuels, which may contribute to the positive T anomaly as well (Dickinson et al., 2021).

The results of this paper are significant, as the potential positive feedbacks described in this paper may prolong wildfires, and therefore also prolong poor air quality conditions inside the southwestern US (Liu & Peng, 2019; O'Neill et al., 2021; Schlosser et al., 2017), as well as other parts of the country (Hung et al., 2020). Additionally, ~~these~~ the significant decreases in

P and/or increases T_s highlighted in this paper occur in heavily populated regions in the southwestern US, including: the San Francisco ~~bay area~~Bay Area, Humboldt County in California, and Washoe County in Nevada. ~~It is possible that these results may also be applicable to other Mediterranean climates, but further research is needed.~~ Therefore, this study highlights an increased need for a curtailment of CO_2 emissions (Ma et al., 2021; Touma et al., 2021) and better land management practices (DellaSala et al., 2022; Minnich et al., 2000; Minnich, 2001), as climate change and land mismanagement have both contributed to the ~~mega-fires~~ large fires in nCA in recent years. Furthermore, as large fires are projected to become more commonplace throughout the 21st century due to these factors (Flannigan et al., 2013; United Nations Environment Programme, 2022), the results of this paper will become more relevant over time as today's 90th percentile fire emission conditions become more common throughout the 21st century. Additionally, this paper highlights the need for more climate models to incorporate feedbacks between wildfires, their aerosols, and semi-direct effects. ~~Models that include interactive emissions of BB aerosols as well as account for the radiative effects of these aerosols on the surface are few and far between, and those that do exist remain in their infancy (Mangeon et al., 2016; Li et al., 2012). Furthermore, as the fire module of these models tend to be unused in the main CMIP simulations, this study highlights a potential deficiency in projections of radiative balance, fire lifetime , and the corresponding air quality impacts in climate model simulations. Therefore, future projections of fire duration , and the associated air quality reduction may be underestimated~~While advances in fire parameterization within climate models have been made (Li et al., 2019; Li & Lawrence, 2017; Mangeon et al., 2016; Allen et al., 2024a), these interactive fire modules are not widely implemented. This study demonstrates that interactive fire modules are a necessity in climate models, as lifetime of fires, and therefore the size and duration of aerosol emission events, are influenced by the fires themselves.

Code availability. Code used to process satellite data will be made available at the following GitHub repository: https://github.com/jgome222/Northern-California-large fires-Associated-with-Decrease-in-Cloud-Cover-Over-the-Southwestern-US

Data availability. All datasets utilized in this analysis are available online. MODIS datasets are available via the 787 NASA Level-1 and Atmosphere Archive & Distribution System (LAADS) Distributed Active Archive 788 Center (DAAC) at https://ladsweb.modaps.eosdis.nasa.gov/archive/allData/61/. CERES datasets can be found at https://ceres.larc.nasa.gov/. AIRS data is available via NASA's Earth Science Data 794 extremes (ESDS) program at https://www.earthdata.nasa.gov/. CALIPSO datasets are available at the Atmospheric Science Data Center (ASDC) at https://asdc.larc.nasa.gov/. GFED4 fire emission data is archived on the GFED4 web page at https://www.globalfiredata.org/. MERRA-2 data can be found on the Goddard Earth Sciences Data and Information Services Center (GES DISC) website at https://disc.gsfc.nasa.gov/datasets?project=MERRA-2.

Appendix A

Symbol
BC
DM
p_s Surface Pressure CERES/GEOS sfc_press AOD
M_{H_2O}
EC Extinction Coefficient CALIPSO Extinction_Coefficient_532_Mean_Elevated_Smoke,Extinction_Coefficient_532_Mean_Polluted_DustExtinctio
T_s
RH
RH_s
CF
CF_{cir}
CF_{lw}
CTH
P
$TOA\ SW$ SWH_{aer}
F_{aer}
TOA_{cld}
SWu
SWd
U_s
Liquid R_{eff}
Ice R_{eff}
LWP
IWP

Table A1. Definition of variables that were derived from satellite observational datasets, as well as the instrument and dataset they are derived from.

Symbol	Definition
nCA	Northern California
nCA-NV	Northern California-Nevada
US	United States
BB	Biomass Burning
~~BC Black Carbon~~ OA	Organic Aerosol
CA	California
SW	Shortwave
AAOD	Absorbing Aerosol Optical Depth
LW	Longwave
TOA	Top of atmosphere
CCN	Cloud Condensation Nuclei
CDF	Cumulative Distribution Function

Table A2. Definitions of abbreviations found throughout the paper that are not associated with a dataset.

Descriptor	Definition
$(DM90)$	Variable stratified by 90th percentile fire dry matter emission anomaly days in nCA
(~~p_s90~~RH_s75)	Variable stratified by ~~90th~~ 75th percentile surface ~~pressure~~ relative humidity anomaly days in nCA-NV
$(DM10)$	Variable stratified by 10th percentile fire dry matter emission anomaly days in nCA
(~~p_s10~~RH_s25)	Variable stratified by ~~10th~~ 25th percentile surface ~~pressure~~ relative humidity anomaly days in nCA-NV
(~~$DM90, p_s90$~~$DM90, RH_s75$)	Variable stratified by 90th percentile fire dry matter emission anomaly days in nCA and ~~90th~~ 75th percentile surface ~~pressure~~ relative humidity anomaly days in nCA-NV
(~~$DM10, p_s90$~~$DM10, RH_s75$)	Variable stratified by 10th percentile fire dry matter emission anomaly days in nCA and ~~90th~~ 75th percentile surface ~~pressure~~ relative humidity anomaly days in nCA-NV
(~~$DM90, p_s10$~~$DM90, RH_s25$)	Variable stratified by 90th percentile fire dry matter emission anomaly days in nCA and ~~10th~~ 25th percentile surface ~~pressure~~ relative humidity anomaly days in nCA-NV
(~~$DM10, p_s10$~~$DM10, RH_s25$)	Variable stratified by 10th percentile fire dry matter emission anomaly days in nCA and ~~10th~~ 25th percentile surface ~~pressure~~ relative humidity anomaly days in nCA-NV
cl	Cloud layer (~~700-250hPa~~850-300 hPa) average of variable
s	Variable measured at the surface
~~ht~~ pho	~~High troposphere (500-200hPa) average of variable~~Hydrophobic aerosol
~~lt~~ phi	~~Low/mid Troposphere (700-500hPa) average of variable~~Hydrophilic aerosol
aer	radiative forcing variable calculated from all-sky minus clear sky products (aerosol only)
cld	radiative forcing variable calculated from all-sky minus no aerosol products (cloud only)
Δ	Difference in variable under different fire and/or ~~pressure~~ relative humidity conditions

Table A3. Definitions of subscripts and other descriptors for variables.

Author contributions. J.L.G. conceived the project, designed the study, performed data analysis and wrote the paper. R.J.A. performed analyses, and wrote the paper. K.L. advised on methods.

Competing interests. The authors declare no competing interests.

Acknowledgements. R.J. Allen is supported by NSF grant AGS-2153486.

References

Abel, S. J., Highwood, E. J., Haywood, J. M., & Stringer, M. A. (2005). The direct radiative effect of biomass burning aerosols over southern Africa. *Atmospheric Chemistry and Physics*, 5(7), 1999–2018.

Ackerman, A. S., Toon, O. B., Stevens, D. E., Heymsfield, A. J., Ramanathan, V., & Welton, E. J. (2000). Reduction of Tropical Cloudiness by Soot. *Science*, 288(5468), 1042–1047.

Adler, R. F., Sapiano, M. R. P., Huffman, G. J., Wang, J.-J., Gu, G., Bolvin, D., Chiu, L., Schneider, U., Becker, A., Nelkin, E., Xie, P., Ferraro, R., & Shin, D.-B. (2018). The Global Precipitation Climatology Project (GPCP) Monthly Analysis (New Version 2.3) and a Review of 2017 Global Precipitation. *Atmosphere*, 9(4), 138.

Ager, A. A., Day, M. A., Alcasena, F. J., Evers, C. R., Short, K. C., & Grenfell, I. (2021). Predicting Paradise: Modeling future wildfire disasters in the western US. *Science of The Total Environment*, 784, 147057.

AIRS Science Team & Texeira, J. (2013). Aqua AIRS Level 3 Standard Daily Product using AIRS IR-only V6.

Allen, R. J., Gomez, J., Horowitz, L. W., & Shevliakova, E. (2024a). Enhanced future vegetation growth with elevated carbon dioxide concentrations could increase fire activity. *Communications Earth & Environment*, 5(1), 1–15. Publisher: Nature Publishing Group.

Allen, R. J., Hassan, T., Randles, C. A., & Su, H. (2019). Enhanced land–sea warming contrast elevates aerosol pollution in a warmer world. *Nature Climate Change*, 9(4), 300–305.

Allen, R. J. & Sherwood, S. C. (2010). Aerosol-cloud semi-direct effect and land-sea temperature contrast in a GCM. *Geophysical Research Letters*, 37(7).

Allen, R. J., Vega, C., Yao, E., & Liu, W. (2024b). Impact of industrial versus biomass burning aerosols on the Atlantic Meridional Overturning Circulation. *npj Climate and Atmospheric Science*, 7(1), 1–16.

Allen, R. J., Zhao, X., Randles, C. A., Kramer, R. J., Samset, B. H., & Smith, C. J. (2023). Surface warming and wetting due to methane's long-wave radiative effects muted by short-wave absorption. *Nature Geoscience*, 16(4), 314–320.

Amiri-Farahani, A., Allen, R. J., Li, K.-F., Nabat, P., & Westervelt, D. M. (2020). A La Niña-Like Climate Response to South African Biomass Burning Aerosol in CESM Simulations. *Journal of Geophysical Research: Atmospheres*, 125(6), e2019JD031832.

Amiri-Farahani, A., Allen, R. J., Neubauer, D., & Lohmann, U. (2017). Impact of Saharan dust on North Atlantic marine stratocumulus clouds: importance of the semidirect effect. *Atmospheric Chemistry and Physics*, 17(10), 6305–6322.

Artaxo, P., Rizzo, L. V., Brito, J. F., Barbosa, H. M. J., Arana, A., Sena, E. T., Cirino, G. G., Bastos, W., Martin, S. T., & Andreae, M. O. (2013). Atmospheric aerosols in Amazonia and land use change: from natural biogenic to biomass burning conditions. *Faraday Discussions*, 165, 203–235.

Brown, P. T., Hanley, H., Mahesh, A., Reed, C., Strenfel, S. J., Davis, S. J., Kochanski, A. K., & Clements, C. B. (2023). Climate warming increases extreme daily wildfire growth risk in California. *Nature*, (pp. 1–7).

Buchard, V., da Silva, A. M., Colarco, P. R., Darmenov, A., Randles, C. A., Govindaraju, R., Torres, O., Campbell, J., & Spurr, R. (2015). Using the OMI aerosol index and absorption aerosol optical depth to evaluate the NASA MERRA Aerosol Reanalysis. *Atmospheric Chemistry and Physics*, 15(10), 5743–5760.

Cape, J. N., Coyle, M., & Dumitrean, P. (2012). The atmospheric lifetime of black carbon. *Atmospheric Environment*, 59, 256–263.

Chen, D., Liu, Z., Schwartz, C. S., Lin, H.-C., Cetola, J. D., Gu, Y., & Xue, L. (2014). The impact of aerosol optical depth assimilation on aerosol forecasts and radiative effects during a wild fire event over the United States. *Geoscientific Model Development*, 7(6), 2709–2715.

Chen, Y., Hall, J., van Wees, D., Andela, N., Hantson, S., Giglio, L., van der Werf, G. R., Morton, D. C., & Randerson, J. T. (2023). Multi-decadal trends and variability in burned area from the fifth version of the Global Fire Emissions Database (GFED5). *Earth System Science Data*, 15(11), 5227–5259. Publisher: Copernicus GmbH.

Cho, C., Kim, S.-W., Choi, W., & Kim, M.-H. (2022). Significant light absorption of brown carbon during the 2020 California wildfires. *Science of The Total Environment*, 813, 152453.

Conrick, R., Mass, C. F., Boomgard-Zagrodnik, J. P., & Ovens, D. (2021). The Influence of Wildfire Smoke on Cloud Microphysics during the September 2020 Pacific Northwest Wildfires. *Weather and Forecasting*, 36(4), 1519–1536.

DellaSala, D. A., Baker, B. C., Hanson, C. T., Ruediger, L., & Baker, W. (2022). Have western USA fire suppression and megafire active management approaches become a contemporary Sisyphus? *Biological Conservation*, 268, 109499.

Dickinson, M. B., Wold, C. E., Butler, B. W., Kremens, R. L., Jimenez, D., Sopko, P., & O'Brien, J. J. (2021). The Wildland Fire Heat Budget—Using Bi-Directional Probes to Measure Sensible Heat Flux and Energy in Surface Fires. *Sensors*, 21(6), 2135.

Doelling, D. (2016). CERES Level 3 SSF1deg-Day Aqua-MODIS HDF file - Edition 4A.

Doelling, D. (2017). CERES Level 3 SYN1DEG-DAYTerra+Aqua HDF4 file - Edition 4A.

Doelling, D. (2023). CERES and GEO-Enhanced TOA, Within-Atmosphere and Surface Fluxes, Clouds and Aerosols Daily Terra-NOAA20 Edition4A.

Eyring, V., Bony, S., Meehl, G. A., Senior, C. A., Stevens, B., Stouffer, R. J., & Taylor, K. E. (2016). Overview of the Coupled Model Intercomparison Project Phase 6 (CMIP6) experimental design and organization. *Geoscientific Model Development*, 9(5), 1937–1958.

Fan, J., Wang, Y., Rosenfeld, D., & Liu, X. (2016). Review of Aerosol–Cloud Interactions: Mechanisms, Significance, and Challenges. *Journal of the Atmospheric Sciences*, 73(11), 4221–4252.

Fasullo, J. T., Rosenbloom, N., Buchholz, R. R., Danabasoglu, G., Lawrence, D. M., & Lamarque, J.-F. (2021). Coupled Climate Responses to Recent Australian Wildfire and COVID-19 Emissions Anomalies Estimated in CESM2. *Geophysical Research Letters*, 48(15), e2021GL093841.

Flannigan, M., Cantin, A. S., de Groot, W. J., Wotton, M., Newbery, A., & Gowman, L. M. (2013). Global wildland fire season severity in the 21st century. *Forest Ecology and Management*, 294, 54–61.

Ford, P. L. & Johnson, G. V. (2006). Effects of dormant- vs. growing-season fire in shortgrass steppe: Biological soil crust and perennial grass responses. *Journal of Arid Environments*, 67(1), 1–14.

Giglio, L., Boschetti, L., Roy, D. P., Humber, M. L., & Justice, C. O. (2018). The Collection 6 MODIS burned area mapping algorithm and product. *Remote Sensing of Environment*, 217, 72–85.

Giglio, L. & Justice, C. (2015). MYD14A1 MODIS/Aqua Thermal Anomalies/Fire Daily L3 Global 1km SIN Grid V006.

Giglio, L., Randerson, J. T., & Van Der Werf, G. R. (2013). Analysis of daily, monthly, and annual burned area using the fourth-generation global fire emissions database (GFED4). *Journal of Geophysical Research: Biogeosciences*, 118(1), 317–328.

Global Modeling And Assimilation Office & Pawson, S. (2015). MERRA-2 inst3_3d_aer_nv: 3d,3-Hourly,Instantaneous,Model-Level,Assimilation,Aerosol Mixing Ratio V5.12.4.

Gomez, J., Allen, R. J., Turnock, S. T., Horowitz, L. W., Tsigaridis, K., Bauer, S. E., Olivié, D., Thomson, E. S., & Ginoux, P. (2023). The projected future degradation in air quality is caused by more abundant natural aerosols in a warmer world. *Communications Earth & Environment*, 4(1), 1–11.

Goren, T. & Rosenfeld, D. (2012). Satellite observations of ship emission induced transitions from broken to closed cell marine stratocumulus over large areas. *Journal of Geophysical Research: Atmospheres*, 117(D17).

Goss, M., Swain, D. L., Abatzoglou, J. T., Sarhadi, A., Kolden, C. A., Williams, A. P., & Diffenbaugh, N. S. (2020). Climate change is increasing the likelihood of extreme autumn wildfire conditions across California. *Environmental Research Letters*, 15(9), 094016.

Han, Q., Rossow, W. B., Chou, J., & Welch, R. M. (1998). Global Survey of the Relationships of Cloud Albedo and Liquid Water Path with Droplet Size Using ISCCP. *Journal of Climate*, 11(7), 1516–1528.

Hansen, J., Sato, M., & Ruedy, R. (1997). Radiative forcing and climate response. *Journal of Geophysical Research: Atmospheres*, 102(D6), 6831–6864.

He, C., Li, Q., Liou, K.-N., Qi, L., Tao, S., & Schwarz, J. P. (2016). Microphysics-based black carbon aging in a global CTM: constraints from HIPPO observations and implications for global black carbon budget. *Atmospheric Chemistry and Physics*, 16(5), 3077–3098.

Helmert, J., Heinold, B., Tegen, I., Hellmuth, O., & Wendisch, M. (2007). On the direct and semidirect effects of Saharan dust over Europe: A modeling study. *Journal of Geophysical Research: Atmospheres*, 112(D13).

Herbert, R. & Stier, P. (2023). Satellite observations of smoke–cloud–radiation interactions over the Amazon rainforest. *Atmospheric Chemistry and Physics*, 23(7), 4595–4616.

Highwood, E. J. & Ryder, C. L. (2014). Radiative Effects of Dust. In P. Knippertz & J.-B. W. Stuut (Eds.), *Mineral Dust: A Key Player in the Earth System* (pp. 267–286). Dordrecht: Springer Netherlands.

Huffman, G. J., Adler, R. F., Morrissey, M. M., Bolvin, D. T., Curtis, S., Joyce, R., McGavock, B., & Susskind, J. (2001). Global Precipitation at One-Degree Daily Resolution from Multisatellite Observations. *Journal of Hydrometeorology*, 2(1), 36–50.

Hung, W.-T., Lu, C.-H. S., Shrestha, B., Lin, H.-C., Lin, C.-A., Grogan, D., Hong, J., Ahmadov, R., James, E., & Joseph, E. (2020). The impacts of transported wildfire smoke aerosols on surface air quality in New York State: A case study in summer 2018. *Atmospheric Environment*, 227, 117415.

Jacobson, M. Z. (2014). Effects of biomass burning on climate, accounting for heat and moisture fluxes, black and brown carbon, and cloud absorption effects. *Journal of Geophysical Research: Atmospheres*, 119(14), 8980–9002.

Kant, S., Sarangi, C., & Wilcox, E. M. (2023). Aerosol processes perturb cloud trends over Bay of Bengal: observational evidence. *npj Climate and Atmospheric Science*, 6(1), 1–8.

Kaufman, Y. J., Koren, I., Remer, L. A., Rosenfeld, D., & Rudich, Y. (2005). The effect of smoke, dust, and pollution aerosol on shallow cloud development over the Atlantic Ocean. *Proceedings of the National Academy of Sciences of the United States of America*, 102(32), 11207–11212.

Keeley, J. E. & Syphard, A. D. (2019). Twenty-first century California, USA, wildfires: fuel-dominated vs. wind-dominated fires. *Fire Ecology*, 15(1), 24.

Khain, A. P. (2009). Notes on state-of-the-art investigations of aerosol effects on precipitation: a critical review. *Environmental Research Letters*, 4(1), 015004.

Koch, D. & Del Genio, A. D. (2010). Black carbon semi-direct effects on cloud cover: review and synthesis. *Atmospheric Chemistry and Physics*, 10(16), 7685–7696.

Kok, J. F., Storelvmo, T., Karydis, V. A., Adebiyi, A. A., Mahowald, N. M., Evan, A. T., He, C., & Leung, D. M. (2023). Mineral dust aerosol impacts on global climate and climate change. *Nature Reviews Earth & Environment*, 4(2), 71–86.

LeNoir, J. S., McConnell, L. L., Fellers, G. M., Cahill, T. M., & Seiber, J. N. (1999). Summertime transport of current-use pesticides from California's Central Valley to the Sierra Nevada Mountain Range, USA. *Environmental Toxicology and Chemistry*, 18(12), 2715–2722.

Levy, R. C., Mattoo, S., Munchak, L. A., Remer, L. A., Sayer, A. M., Patadia, F., & Hsu, N. C. (2013). The Collection 6 MODIS aerosol products over land and ocean. *Atmospheric Measurement Techniques*, 6(11), 2989–3034.

Li, F. & Lawrence, D. M. (2017). Role of Fire in the Global Land Water Budget during the Twentieth Century due to Changing Ecosystems. *Journal of Climate*, 30(6), 1893–1908.

Li, F., Val Martin, M., Andreae, M. O., Arneth, A., Hantson, S., Kaiser, J. W., Lasslop, G., Yue, C., Bachelet, D., Forrest, M., Kluzek, E., Liu, X., Mangeon, S., Melton, J. R., Ward, D. S., Darmenov, A., Hickler, T., Ichoku, C., Magi, B. I., Sitch, S., van der Werf, G. R., Wiedinmyer, C., & Rabin, S. S. (2019). Historical (1700–2012) global multi-model estimates of the fire emissions from the Fire Modeling Intercomparison Project (FireMIP). *Atmospheric Chemistry and Physics*, 19(19), 12545–12567.

Li, F., Zeng, X. D., & Levis, S. (2012). A process-based fire parameterization of intermediate complexity in a Dynamic Global Vegetation Model. *Biogeosciences*, 9(7), 2761–2780.

Li, S. & Banerjee, T. (2021). Spatial and temporal pattern of wildfires in California from 2000 to 2019. *Scientific Reports*, 11(1), 8779.

Liu, J. C. & Peng, R. D. (2019). The impact of wildfire smoke on compositions of fine particulate matter by ecoregion in the Western US. *Journal of Exposure Science & Environmental Epidemiology*, 29(6), 765–776.

Liu, Z., Hu, M., Hu, Y., & Wang, G. (2018). Estimation of net primary productivity of forests by modified CASA models and remotely sensed data. *International Journal of Remote Sensing*, 39(4), 1092–1116.

Lohmann, U., Friebel, F., Kanji, Z. A., Mahrt, F., Mensah, A. A., & Neubauer, D. (2020). Future warming exacerbated by aged-soot effect on cloud formation. *Nature Geoscience*, 13(10), 674–680.

Ma, W., Zhai, L., Pivovaroff, A., Shuman, J., Buotte, P., Ding, J., Christoffersen, B., Knox, R., Moritz, M., Fisher, R. A., Koven, C. D., Kueppers, L., & Xu, C. (2021). Assessing climate change impacts on live fuel moisture and wildfire risk using a hydrodynamic vegetation model. *Biogeosciences*, 18(13), 4005–4020.

Mangeon, S., Voulgarakis, A., Gilham, R., Harper, A., Sitch, S., & Folberth, G. (2016). INFERNO: a fire and emissions scheme for the UK Met Office's Unified Model. *Geoscientific Model Development*, 9(8), 2685–2700.

Martins, J. V., Marshak, A., Remer, L. A., Rosenfeld, D., Kaufman, Y. J., Fernandez-Borda, R., Koren, I., Correia, A. L., Zubko, V., & Artaxo, P. (2011). Remote sensing the vertical profile of cloud droplet effective radius, thermodynamic phase, and temperature. *Atmospheric Chemistry and Physics*, 11(18), 9485–9501.

Minnich, R. A. (2001). An Integrated Model of Two Fire Regimes. *Conservation Biology*, 15(6), 1549–1553.

Minnich, R. A., Barbour, M. G., Burk, J. H., & Sosa-Ramírez, J. (2000). Californian mixed-conifer forests under unmanaged fire regimes in the Sierra San Pedro Mártir, Baja California, Mexico. *Journal of Biogeography*, 27(1), 105–129.

Minnich, R. A. & Chou, Y. H. (1997). Wildland Fire Patch Dynamics in the Chaparral of Southern California and Northern Baja California. *International Journal of Wildland Fire*, 7(3), 221–248.

MODIS Atmosphere Science Team (2017). MYD08_d3 MODIS/Aqua Aerosol Cloud Water Vapor Ozone Daily L3 Global 1Deg CMG.

Nguyen, L. S. P., Huang, H.-Y., Lei, T. L., Bui, T. T., Wang, S.-H., Chi, K. H., Sheu, G.-R., Lee, C.-T., Ou-Yang, C.-F., & Lin, N.-H. (2020). Characterizing a landmark biomass-burning event and its implication for aging processes during long-range transport. *Atmospheric Environment*, 241, 117766.

Ogren, J. A. & Charlson, R. J. (1983). Elemental carbon in the atmosphere: cycle and lifetime. *Tellus B*, 35B(4), 241–254.

Ou, S.-c. & Liou, K.-N. (1995). Ice microphysics and climatic temperature feedback. *Atmospheric Research*, 35(2), 127–138.

O'Neill, S. M., Diao, M., Raffuse, S., Al-Hamdan, M., Barik, M., Jia, Y., Reid, S., Zou, Y., Tong, D., West, J. J., Wilkins, J., Marsha, A., Freedman, F., Vargo, J., Larkin, N. K., Alvarado, E., & Loesche, P. (2021). A multi-analysis approach for estimating regional health impacts from the 2017 Northern California wildfires. *Journal of the Air & Waste Management Association*, 71(7), 791–814.

Palinkas, L. A. (2020). The California Wildfires. In L. A. Palinkas (Ed.), *Global Climate Change, Population Displacement, and Public Health: The Next Wave of Migration* (pp. 53–67). Cham: Springer International Publishing.

Peterson, D., Wang, J., Ichoku, C., Hyer, E., & Ambrosia, V. (2013). A sub-pixel-based calculation of fire radiative power from MODIS observations: 1: Algorithm development and initial assessment. *Remote Sensing of Environment*, 129, 262–279.

Platnick, S., King, M., Ackerman, S., Menzel, W., Baum, B., Riedi, J., & Frey, R. (2003). The MODIS cloud products: algorithms and examples from Terra. *IEEE Transactions on Geoscience and Remote Sensing*, 41(2), 459–473.

Platnick, S., Meyer, K. G., King, M. D., Wind, G., Amarasinghe, N., Marchant, B., Arnold, G. T., Zhang, Z., Hubanks, P. A., Holz, R. E., Yang, P., Ridgway, W. L., & Riedi, J. (2017). The MODIS Cloud Optical and Microphysical Products: Collection 6 Updates and Examples From Terra and Aqua. *IEEE Transactions on Geoscience and Remote Sensing*, 55(1), 502–525.

Raga, G. B., Baumgardner, D., Rios, B., Díaz-Esteban, Y., Jaramillo, A., Gallagher, M., Sauvage, B., Wolff, P., & Lloyd, G. (2022). High concentrations of ice crystals in upper-tropospheric tropical clouds: is there a link to biomass and fossil fuel combustion? *Atmospheric Chemistry and Physics*, 22(4), 2269–2292.

Randerson, J., van der Werf, G., Giglio, L., Collatz, G., & Kasibhatla, P. (2017). Global Fire Emissions Database, Version 4.1 (GFEDv4). (pp. 1925.7122549999906 MB).

Randles, C. A., Silva, A. M. d., Buchard, V., Colarco, P. R., Darmenov, A., Govindaraju, R., Smirnov, A., Holben, B., Ferrare, R., Hair, J., Shinozuka, Y., & Flynn, C. J. (2017). The MERRA-2 Aerosol Reanalysis, 1980 Onward. Part I: System Description and Data Assimilation Evaluation. *Journal of Climate*, 30(17), 6823–6850.

Ruffault, J., Curt, T., Moron, V., Trigo, R. M., Mouillot, F., Koutsias, N., Pimont, F., Martin-StPaul, N., Barbero, R., Dupuy, J.-L., Russo, A., & Belhadj-Khedher, C. (2020). Increased likelihood of heat-induced large wildfires in the Mediterranean Basin. *Scientific Reports*, 10(1), 13790.

Sakaeda, N., Wood, R., & Rasch, P. J. (2011). Direct and semidirect aerosol effects of southern African biomass burning aerosol. *Journal of Geophysical Research: Atmospheres*, 116(D12).

Salomonson, V., Barnes, W., Xiong, J., Kempler, S., & Masuoka, E. (2002). An overview of the Earth Observing System MODIS instrument and associated data systems performance. In *IEEE International Geoscience and Remote Sensing Symposium*, volume 2 (pp. 1174–1176 vol.2).

Samset, B. H. (2022). Aerosol absorption has an underappreciated role in historical precipitation change. *Communications Earth & Environment*, 3(1), 1–8.

Sand, M., Samset, B. H., Tsigaridis, K., Bauer, S. E., & Myhre, G. (2020). Black Carbon and Precipitation: An Energetics Perspective. *Journal of Geophysical Research: Atmospheres*, 125(13), e2019JD032239.

Schlosser, J. S., Braun, R. A., Bradley, T., Dadashazar, H., MacDonald, A. B., Aldhaif, A. A., Aghdam, M. A., Mardi, A. H., Xian, P., & Sorooshian, A. (2017). Analysis of aerosol composition data for western United States wildfires between 2005 and 2015: Dust emissions, chloride depletion, and most enhanced aerosol constituents. *Journal of Geophysical Research: Atmospheres*, 122(16), 8951–8966.

Shi, G., Yan, H., Zhang, W., Dodson, J., Heijnis, H., & Burrows, M. (2021). Rapid warming has resulted in more wildfires in northeastern Australia. *Science of The Total Environment*, 771, 144888.

Smith, C. J., Kramer, R. J., Myhre, G., Forster, P. M., Soden, B. J., Andrews, T., Boucher, O., Faluvegi, G., Fläschner, D., Hodnebrog, Ø., Kasoar, M., Kharin, V., Kirkevåg, A., Lamarque, J.-F., Mülmenstädt, J., Olivié, D., Richardson, T., Samset, B. H., Shindell, D., Stier, P., Takemura, T., Voulgarakis, A., & Watson-Parris, D. (2018). Understanding Rapid Adjustments to Diverse Forcing Agents. *Geophysical Research Letters*, 45(21), 12,023–12,031.

Stjern, C. W., Samset, B. H., Myhre, G., Forster, P. M., Hodnebrog, Ø., Andrews, T., Boucher, O., Faluvegi, G., Iversen, T., Kasoar, M., Kharin, V., Kirkevåg, A., Lamarque, J.-F., Olivié, D., Richardson, T., Shawki, D., Shindell, D., Smith, C. J., Takemura, T., & Voulgarakis, A. (2017). Rapid Adjustments Cause Weak Surface Temperature Response to Increased Black Carbon Concentrations. *Journal of Geophysical Research: Atmospheres*, 122(21), 11,462–11,481.

Tackett, J. L., Winker, D. M., Getzewich, B. J., Vaughan, M. A., Young, S. A., & Kar, J. (2018). CALIPSO lidar level 3 aerosol profile product: version 3 algorithm design. *Atmospheric Measurement Techniques*, 11(7), 4129–4152.

Thornhill, G. D., Ryder, C. L., Highwood, E. J., Shaffrey, L. C., & Johnson, B. T. (2018). The effect of South American biomass burning aerosol emissions on the regional climate. *Atmospheric Chemistry and Physics*, 18(8), 5321–5342.

Touma, D., Stevenson, S., Lehner, F., & Coats, S. (2021). Human-driven greenhouse gas and aerosol emissions cause distinct regional impacts on extreme fire weather. *Nature Communications*, 12(1), 212.

Tsikerdekis, A., Zanis, P., Georgoulias, A. K., Alexandri, G., Katragkou, E., Karacostas, T., & Solmon, F. (2019). Direct and semi-direct radiative effect of North African dust in present and future regional climate simulations. *Climate Dynamics*, 53(7), 4311–4336.

Twohy, C. H., Toohey, D. W., Levin, E. J. T., DeMott, P. J., Rainwater, B., Garofalo, L. A., Pothier, M. A., Farmer, D. K., Kreidenweis, S. M., Pokhrel, R. P., Murphy, S. M., Reeves, J. M., Moore, K. A., & Fischer, E. V. (2021). Biomass Burning Smoke and Its Influence on Clouds Over the Western U. S. *Geophysical Research Letters*, 48(15), e2021GL094224.

United Nations Environment Programme (2022). Spreading like Wildfire – The Rising Threat of Extraordinary Landscape Fires.

Urbanski, S. P. (2013). Combustion efficiency and emission factors for wildfire-season fires in mixed conifer forests of the northern Rocky Mountains, US. *Atmospheric Chemistry and Physics*, 13(14), 7241–7262.

Urbanski, S. P., Hao, W. M., & Nordgren, B. (2011). The wildland fire emission inventory: western United States emission estimates and an evaluation of uncertainty. *Atmospheric Chemistry and Physics*, 11(24), 12973–13000.

van der Werf, G. R., Randerson, J. T., Giglio, L., van Leeuwen, T. T., Chen, Y., Rogers, B. M., Mu, M., van Marle, M. J. E., Morton, D. C., Collatz, G. J., Yokelson, R. J., & Kasibhatla, P. S. (2017). Global fire emissions estimates during 1997–2016. *Earth System Science Data*, 9(2), 697–720.

Varga, K., Jones, C., Trugman, A., Carvalho, L. M. V., McLoughlin, N., Seto, D., Thompson, C., & Daum, K. (2022). Megafires in a Warming World: What Wildfire Risk Factors Led to California's Largest Recorded Wildfire. *Fire*, 5(1), 16.

Wagenbrenner, N. S., Chung, S. H., & Lamb, B. K. (2017). A large source of dust missing in Particulate Matter emission inventories? Wind erosion of post-fire landscapes. *Elementa: Science of the Anthropocene*, 5, 2.

Wagenbrenner, N. S., Germino, M. J., Lamb, B. K., Robichaud, P. R., & Foltz, R. B. (2013). Wind erosion from a sagebrush steppe burned by wildfire: Measurements of PM10 and total horizontal sediment flux. *Aeolian Research*, 10, 25–36.

Wagner, R., Jähn, M., & Schepanski, K. (2018). Wildfires as a source of airborne mineral dust – revisiting a conceptual model using large-eddy simulation (LES). *Atmospheric Chemistry and Physics*, 18(16), 11863–11884.

Wagner, R., Schepanski, K., & Klose, M. (2021). The Dust Emission Potential of Agricultural-Like Fires—Theoretical Estimates From Two Conceptually Different Dust Emission Parameterizations. *Journal of Geophysical Research: Atmospheres*, 126(18), e2020JD034355.

Wei, J., Li, Z., Peng, Y., & Sun, L. (2019). MODIS Collection 6.1 aerosol optical depth products over land and ocean: validation and comparison. *Atmospheric Environment*, 201, 428–440.

Wielicki, B., Barkstrom, B., Baum, B., Charlock, T., Green, R., Kratz, D., Lee, R., Minnis, P., Smith, G., Wong, T., Young, D., Cess, R., Coakley, J., Crommelynck, D., Donner, L., Kandel, R., King, M., Miller, A., Ramanathan, V., Randall, D., Stowe, L., & Welch, R. (1998).

Clouds and the Earth's Radiant Energy System (CERES): algorithm overview. *IEEE Transactions on Geoscience and Remote Sensing*, 36(4), 1127–1141.

Wilcox, E. M. (2012). Direct and semi-direct radiative forcing of smoke aerosols over clouds. *Atmospheric Chemistry and Physics*, 12(1), 139–149.

Wilmot, T. Y., Mallia, D. V., Hallar, A. G., & Lin, J. C. (2022). Wildfire plumes in the Western US are reaching greater heights and injecting more aerosols aloft as wildfire activity intensifies. *Scientific Reports*, 12(1), 12400.

Winker, D. (2019). CALIPSO Lidar Level 3 Tropospheric Aerosol Profiles, All Sky Data, Standard V4-20.

Yu, J., Jiang, X., Zeng, Z.-C., & Yung, Y. L. (2024). Fire monitoring and detection using brightness-temperature difference and water vapor emission from the atmospheric infrared sounder. *Journal of Quantitative Spectroscopy and Radiative Transfer*, 317, 108930.

Yu, Y. & Ginoux, P. (2022). Enhanced dust emission following large wildfires due to vegetation disturbance. *Nature Geoscience*, 15(11), 878–884.

Zaremba, L. L. & Carroll, J. J. (1999). Summer Wind Flow Regimes over the Sacramento Valley. *Journal of Applied Meteorology and Climatology*, 38(10), 1463–1473.

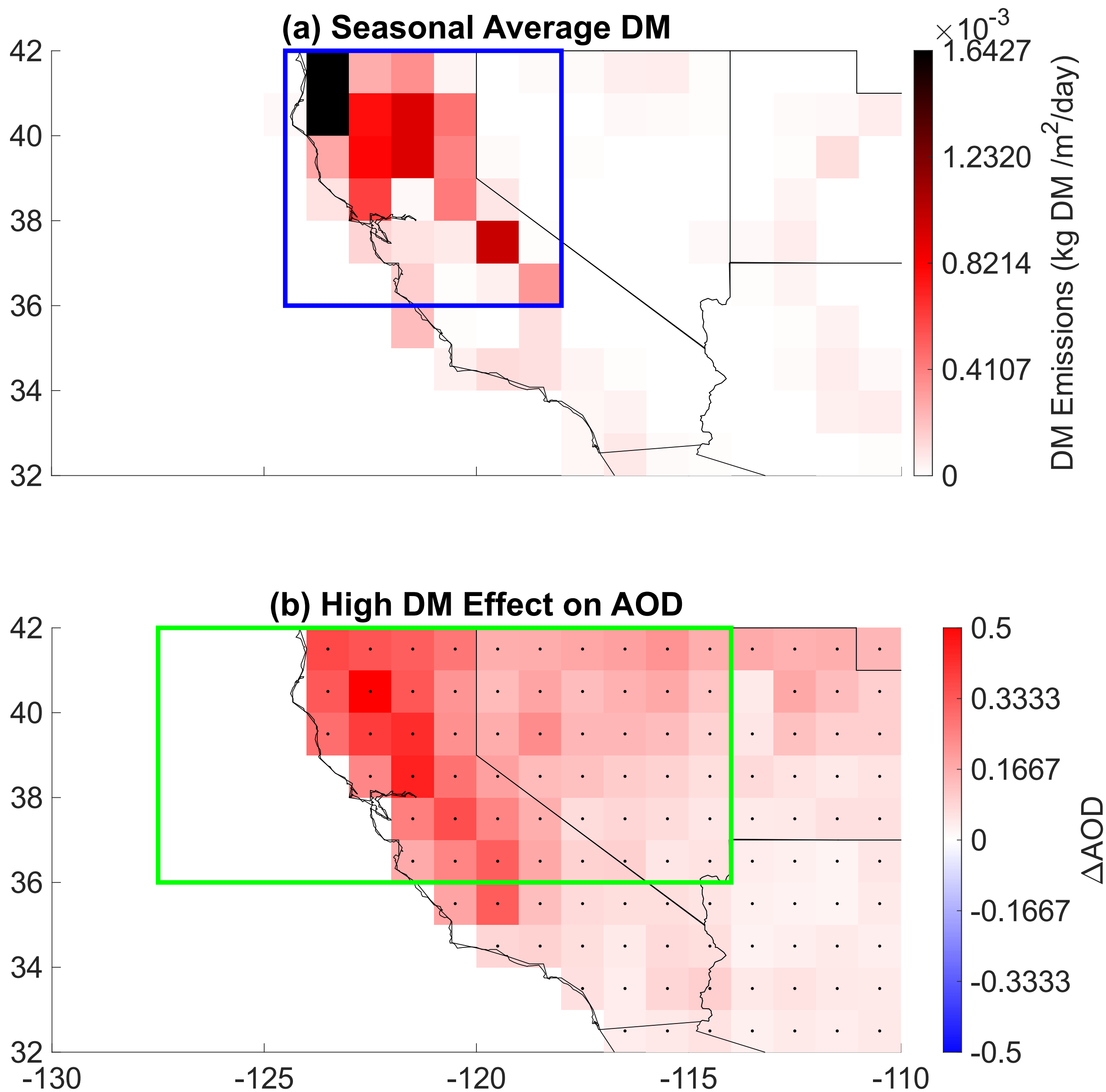

Figure 1. Distribution of fires and the corresponding aerosol optical depth AOD anomaly impacts during the fire season. (a) 2003-2022 average daily fire dry matter DM emissions for the southwestern United States during the fire season (June-October). Blue box signifies the nCA (northern California) region, where average daily fire emissions are the highest. (b) 2003-2022 June-October daily ~~Deep Blue~~ MODIS Aerosol optical depth (AOD) difference between average AOD on 90th percentile DM ($DM90$) and average AOD on 10th percentile DM ($DM10$) days within the 2003-2022 June-October time ~~frame~~period. ΔAOD represents $AOD(DM90) - AOD(DM10)$. Green box symbolizes the nCA-NV (northern California-Nevada) region, where increases in AOD and changes in cloud properties (~~Figure 9)~~ Figure 11) are most significant. Black dots represent statistically significant differences at 90% confidence according to a two-tailed test.

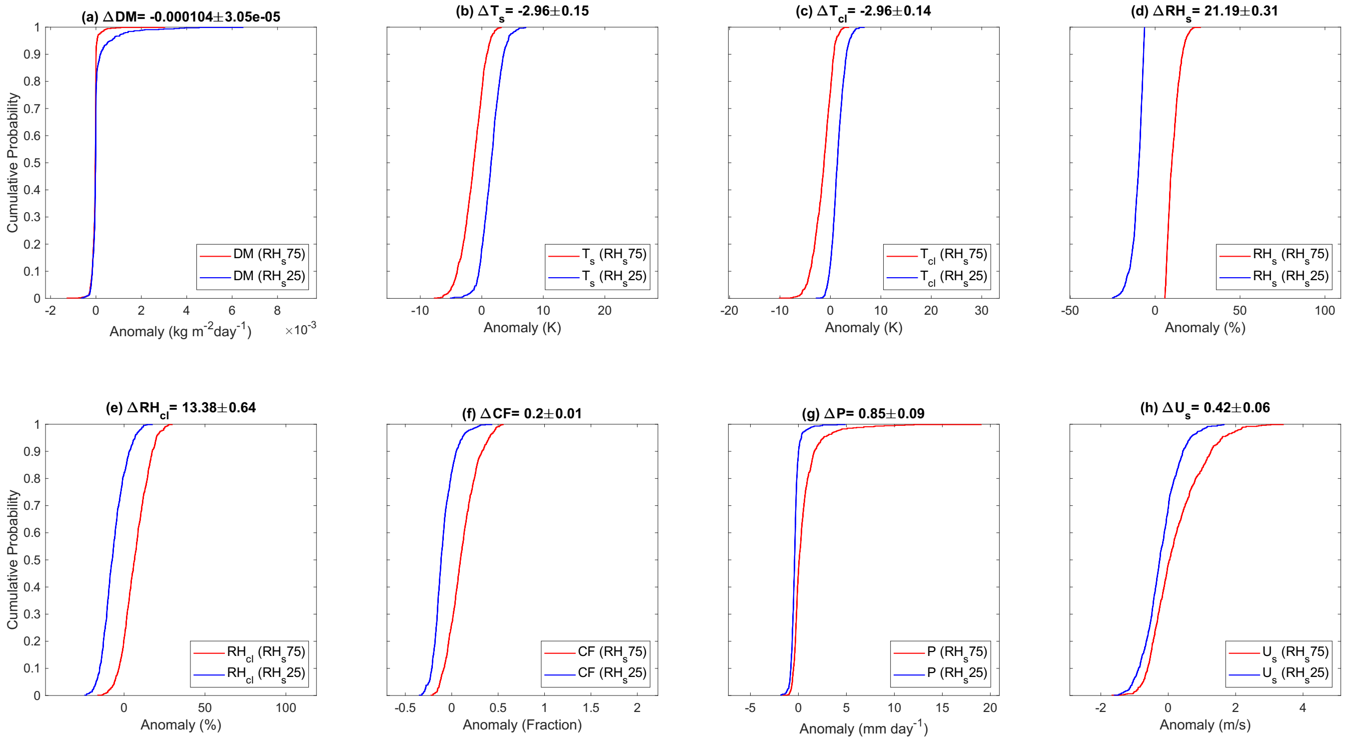

Dependence of meteorological variables on high versus low surface ~~pressure~~relative humidity RH_s during the fire season. Regional average cumulative distribution functions (CDFs) for variable anomalies stratified by ~~90th~~ 75th percentile surface ~~pressure~~ relative humidity (~~p_s90~~RH_s75) days (red) and ~~10th~~ 25th percentile (~~p_s10~~RH_s25) (blue) days within the 2003-2022 June-October time ~~frame~~period. Variables depicted include (a) northern California (nCA) fire dry matter (DM) emissions, (b) ~~northern California-Nevada (nCA-NV)~~ southwestern US surface temperature T_s, (c) nCA-NV cloud layer (~~700-250hPa~~850-300 hPa) average temperature T_{cl}, (d) ~~nCA-NV~~ southwestern US surface relative humidity RH_s, (e) ~~nCA-NV~~ southwestern US cloud layer average relative humidity RH_{cl}, (f) ~~nCA-NV~~ southwestern US cloud fraction CF, (g) ~~nCA-NV~~ southwestern US precipitation P, and (h) ~~nCA-NV~~ southwestern US surface wind speed U. Δ represents the difference between the variable's average anomaly for ~~p_s90~~ RH_s75 and ~~p_s10~~ RH_s25 days.

Dependence of meteorological variables on high versus low surface ~~pressure~~relative humidity RH_s during the fire season. Regional average cumulative distribution functions (CDFs) for variable anomalies stratified by ~~90th~~ 75th percentile surface ~~pressure~~ relative humidity (~~p_s90~~RH_s75) days (red) and ~~10th~~ 25th percentile (~~p_s10~~RH_s25) (blue) days within the 2003-2022 June-October time ~~frame~~period. Variables depicted include (a) northern California (nCA) fire dry matter (DM) emissions, (b) ~~northern California-Nevada (nCA-NV)~~ southwestern US surface temperature T_s, (c) nCA-NV cloud layer (~~700-250hPa~~850-300 hPa) average temperature T_{cl}, (d) ~~nCA-NV~~ southwestern US surface relative humidity RH_s, (e) ~~nCA-NV~~ southwestern US cloud layer average relative humidity RH_{cl}, (f) ~~nCA-NV~~ southwestern US cloud fraction CF, (g) ~~nCA-NV~~ southwestern US precipitation P, and (h) ~~nCA-NV~~ southwestern US surface wind speed U. Δ represents the difference between the variable's average anomaly for ~~p_s90~~ RH_s75 and ~~p_s10~~ RH_s25 days.

Figure 2. ~~Aerosols extinction coefficient EC profiles on high minus low fire months. Difference in 2006-2021 northern California/Nevada (nCA-NV) regional average CALIPSO EC profiles that occur in 90th percentile northern California (nCA) fire emission months and 10th percentile nCA fire emission months within the 2006-2021 June-October time frame. Blue represents the smoke EC profile, and gold represents the polluted dust EC profile. (a,c) depict the daytime CALIPSO retrievals, while (b,d) depict nighttime CALIPSO retrievals. (a) and (b) display the entire vertical EC profiles, while (c,d) display the profiles in the high troposphere (pressures less than 500hPa). Error bars represent standard errors.~~

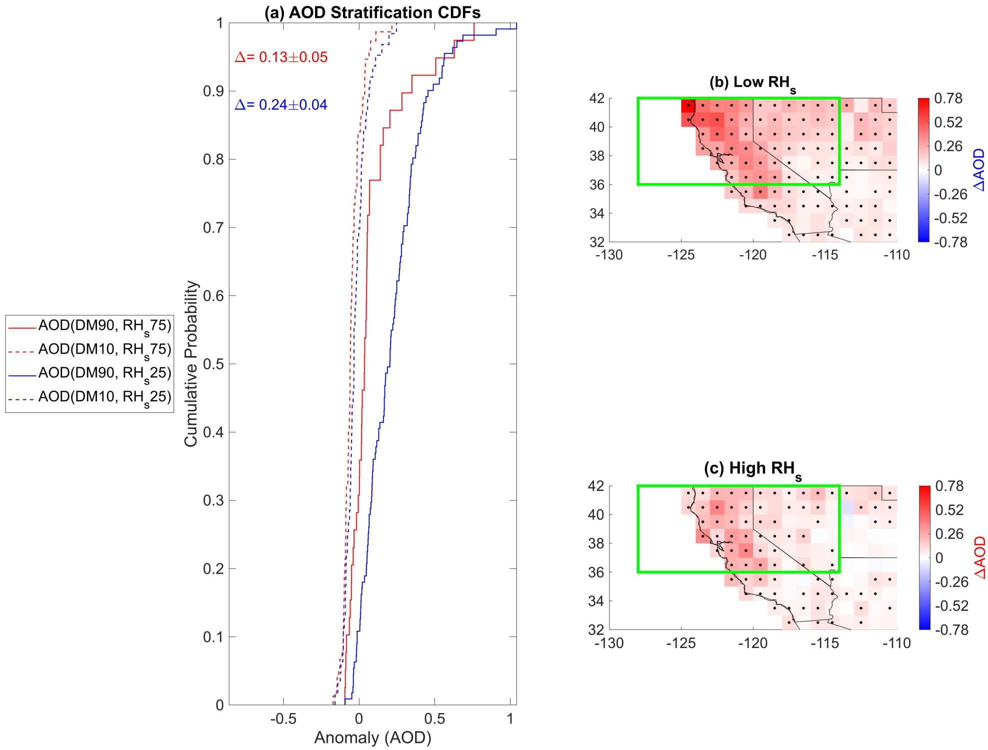

Figure 3. Difference in ~~aerosol optical depth~~ AOD anomalies on high and low ~~surface pressure p_s~~ RH_s days during the fire season. Daily ~~northern California-Nevada (~~nCA-NV ~~)~~ AOD anomalies stratified by ~~p_s~~ nCA-NV RH_s and ~~northern California (~~nCA ~~) fire dry matter~~ DM ~~emission~~ extremes within the 2003-2022 June-October time ~~frame~~period. (a) displays cumulative distribution functions for daily June-October 2003-2022 daily northern California-Nevada ~~(~~nCA-NV ~~)~~ AOD stratified by high (90th percentile) nCA DM emissions and high nCA-NV ~~p_s~~ RH_s $AOD($~~$DM90, p_s90$~~$DM90, RH_s75)$ (solid red line), low (10th percentile) DM and high ~~p_s~~ RH_s $AOD(DM10,$~~p_s90~~$RH_s75)$ (dashed red), high DM/low ~~p_s~~ RH_s $AOD($~~$DM90, p_s10$~~$DM90, RH_s25)$ (solid blue line), and low nCA DM/low ~~p_s~~ RH_s $AOD($~~$DM10, p_s10$~~$DM10, RH_s25)$ (dashed blue line). The red ΔAOD represents the difference between the solid red and dashed red line $AOD($~~$DM90, p_s90$~~$DM90, RH_s75)$-$AOD($~~$DM10, p_s90$~~$DM10, RH_s75)$ and the blue ΔAOD represents the difference between the solid and dashed blue lines $AOD($~~$DM90, p_s10$~~$DM90, RH_s25)$-$AOD($~~$DM10, p_s10$~~$DM10, RH_s25)$. (b) Depicts a map of $AOD($~~$DM90, p_s10$~~$DM90, RH_s25)$-$AOD($~~$DM10, p_s10$~~$DM10, RH_s25)$~~with the nCA-NV region highlighted in the green box~~. Pearson cross correlation coefficient r between ΔAOD and nCA DM emissions is depicted in the top left corner. (c) Depicts a map of average $AOD($~~$DM90, p_s90$~~$DM90, RH_s75)$-$AOD($~~$DM10, p_s90$~~$DM10, RH_s75)$. Black dots in (b),(c) represent statistically significant differences at the 90% confidence interval according to a two-tailed test.

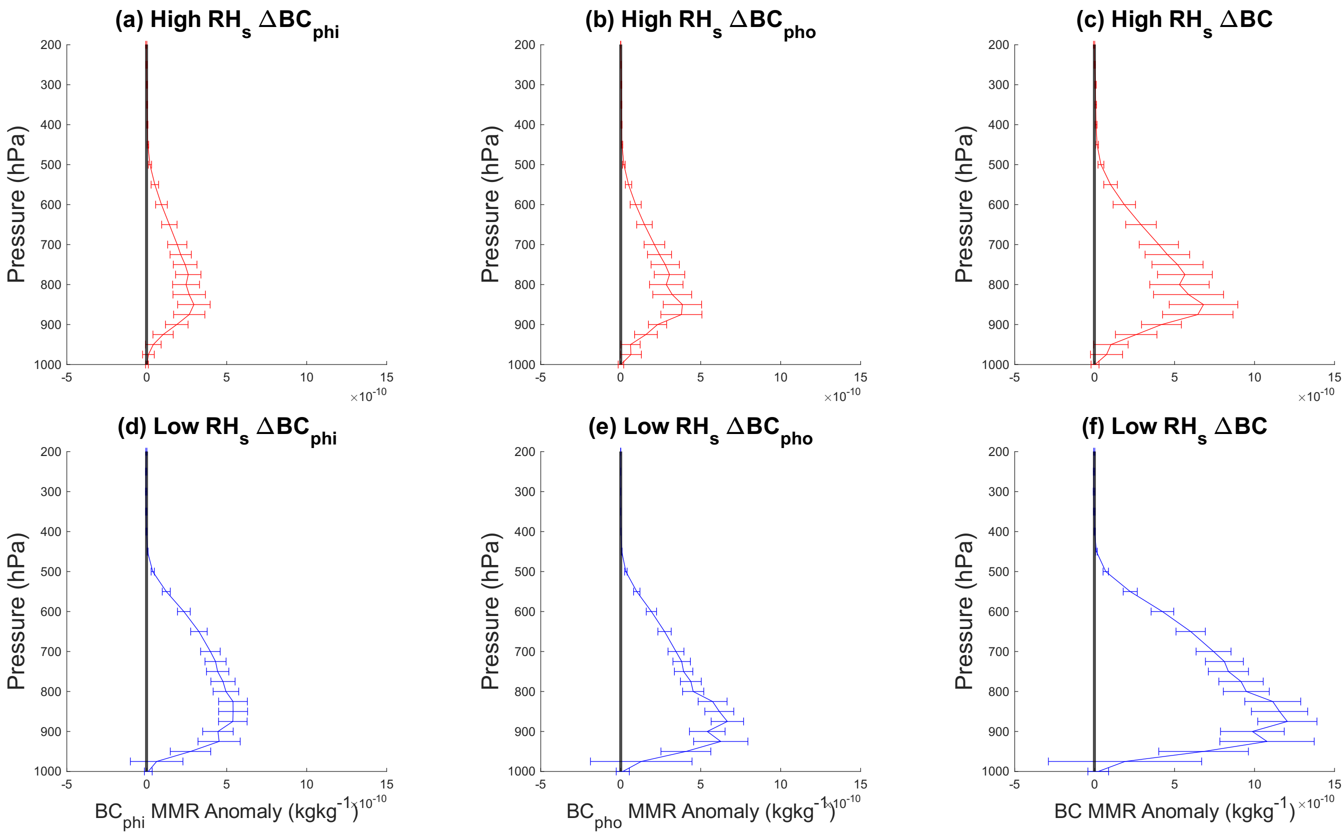

Figure 4. Difference in MERRA-2 black carbon BC profiles on high vs low fire days stratified by differing RH_s conditions in the nCA-NV region in the 2003-2022 June-October time period. Profiles of both aged hydrophilic black carbon BC_{phi} (a,d) as well as freshly emitted hydrophobic black carbon BC_{pho} (b,e) are depicted in addition to total BC (c,f). All types of BC have significant anomalies from 850-300 hPa under both high RH_s (a-c) as well as low RH_s conditions (d-f).

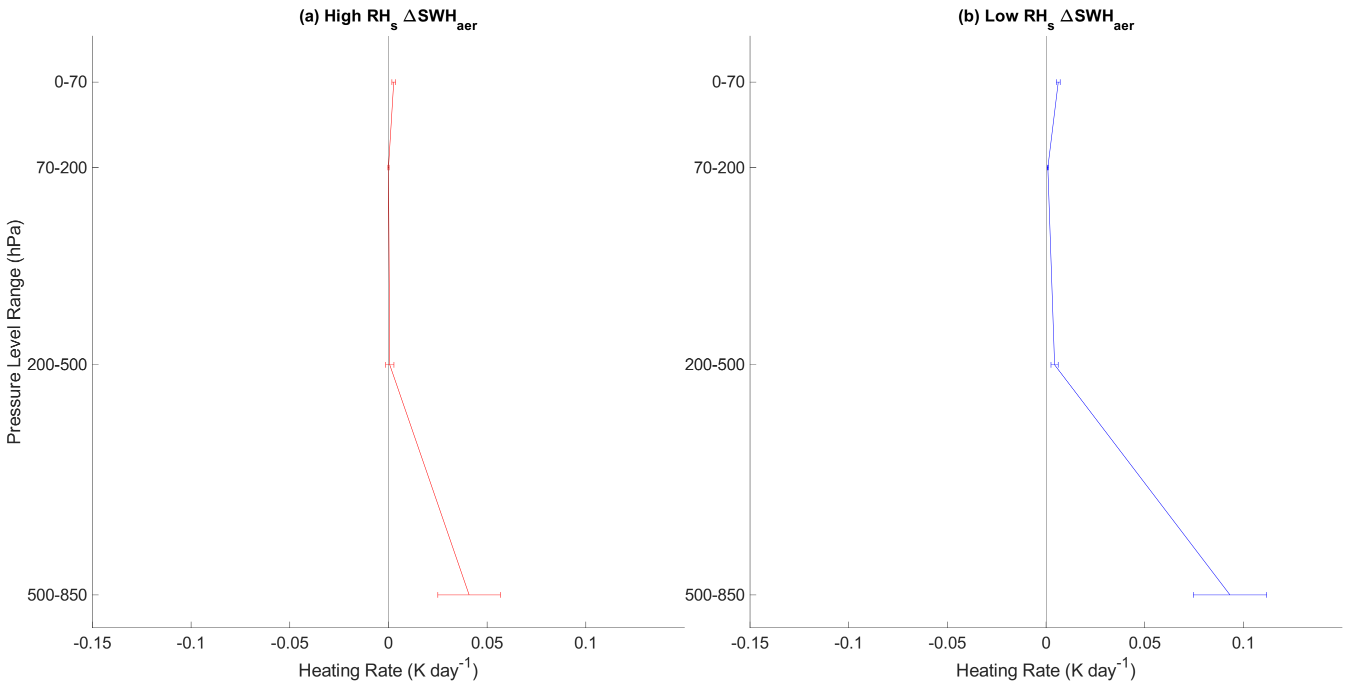

Figure 5. High minus low DM days regional average aerosol-only shortwave heating rate SWH_{aer} profiles under differing RH_s conditions in the 2003-2022 June-October time period. There is a significant shortwave aerosol heating rate from 850-500 hPa under both high RH_s conditions (a) as well as low RH_s conditions (b).

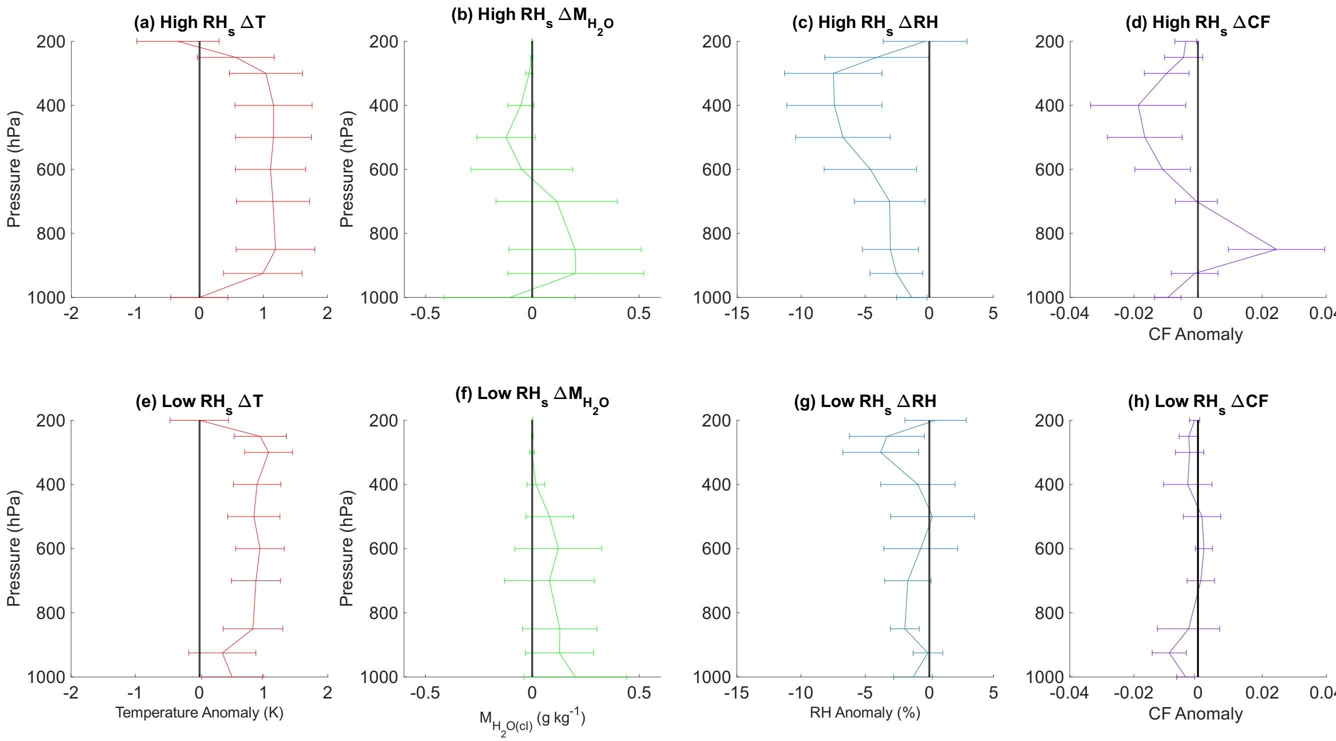

Figure 6. Responses in AIRS temperature T, water mass mixing ratio M_{H_2O}, ~~and~~ relative humidity RH, and cloud fraction CF profiles to large fires under high and low ~~surface pressure p_s~~ RH_s extremes during the fire season. ~~Northern California-Nevada~~ nCA-NV regional-temporal average differences in T, water mass mixing ratio M_{H_2O} and relative humidity RH profiles ~~between~~ for under high ~~(90th percentile) and~~ minus low ~~(10th percentile) northern California fire dry matter emissions~~ DM ~~anomalies~~ conditions stratified by ~~days of high~~ RH_s75 (a-d) and ~~low p_s anomaly extremes~~ RH_s25 (e-h) in the 2002-2023 fire season (June-October) time ~~frame~~period. ~~(a,b,c) represent T, M_{H_2O}, and RH differences between high and low fire days on high p_s days. (d,e,f) represent T, M_{H_2O}, and RH differences between high and low fire days on low p_s days.~~ Error bars represent ~~standard error~~the 90% confidence interval.

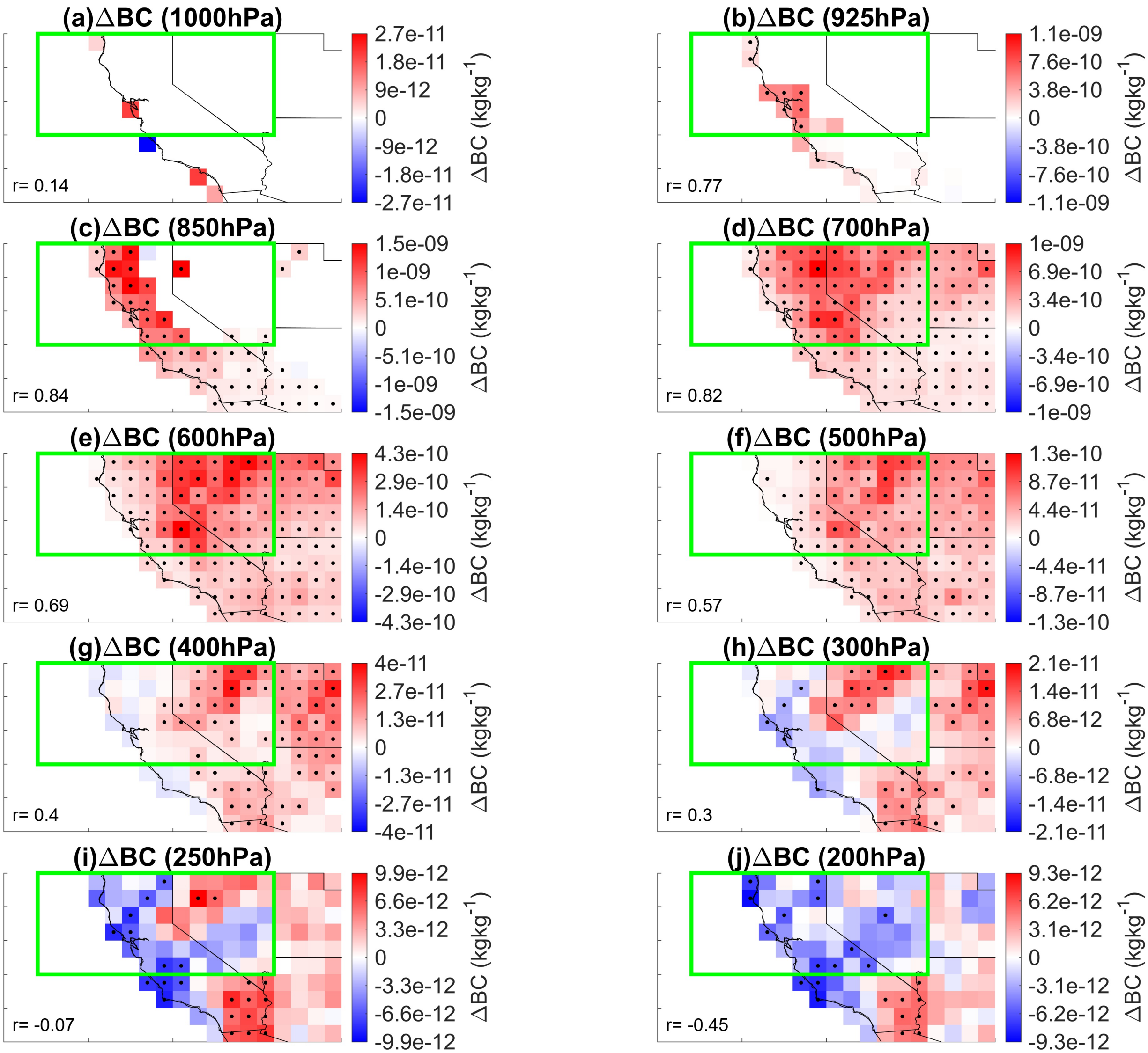

Figure 7. Contributions of specific humidity and temperature to changes in relative humidity in the high and low troposphere. Average high (90th percentile) High minus low (10th percentile) fire dry matter emission DM days (in the 2002-2022 June-October timeframe) water mass mixing ratio, temperature, and relative humidity MERRA-2 BC anomalies in the high (500-200hPa) and low/mid (700-500 hPa) troposphere during low surface at all AIRS pressure p_s. Low levels from 1000 hPa to 200 hPa (10th percentilea-j) pressure extreme 90th minus 10th percentile DM seasonal average anomalies for (a) under high troposphere water mass mixing ratio $M_{H_2O(ht)}$, (b) high troposphere temperature T_{ht}, (c) high troposphere relative humidity RH_{ht}, (d) low/mid troposphere water mass mixing ratio $M_{H_2O(lt)}$, (e) low/mid troposphere temperature T_{lt}, and (f) high troposphere relative humidity RH_{lt} RH_s conditions in the 2003-2022 June-October time period. Black dots represent statistically significant differences indicate statistical significance at the 90% confidence intervalaccording to a two-tailed test. Green box represents northern California-Nevada region. r-value represents r values indicate spatial Pearson cross correlation coefficient correlations between the given variable total BC and aerosol optical depth at zero lagMODIS AOD.

Dependence of meteorological variables to high versus low surface pressure p_s and fires. Cumulative distribution functions (CDFs) for meteorological daily variables' regional average anomalies over the northern California-Nevada (nCA-NV) region in the 2003-2022 June-October timeframe. Solid red line signifies variable anomalies are stratified by high (90th percentile) northern California (nCA) fire dry matter emission DM and high p_s anomaly days ($DM90, p_s90$). The dashed red line signifies variable anomalies are stratified by low (10th percentile) nCA DM and high p_s anomaly days ($DM10, p_s90$). The solid blue line represents variable anomalies are stratified by high nCA DM and 10th percentile p_s anomaly days ($DM90, p_s10$). The dashed blue line symbolizes variable anomalies are stratified by low DM and low p_s anomaly days ($DM10, p_s10$). Variables depicted include (a) cirrus cloud fraction CF_{cir}, (b) liquid water cloud fraction CF_{lw}, (c) cloud fraction CF, (d) cloud top height CTH, (e) precipitation P, and (f) outgoing top of atmosphere shortwave flux $TOA\ SW$. The red Δ represents the differences in the mean of the solid red and dashed red lines ($DM90, p_s90$)-($DM10, p_s90$). The blue Δ represents the differences in the mean of the solid blue and dashed blue lines ($DM90, p_s10$)-($DM10, p_s10$).

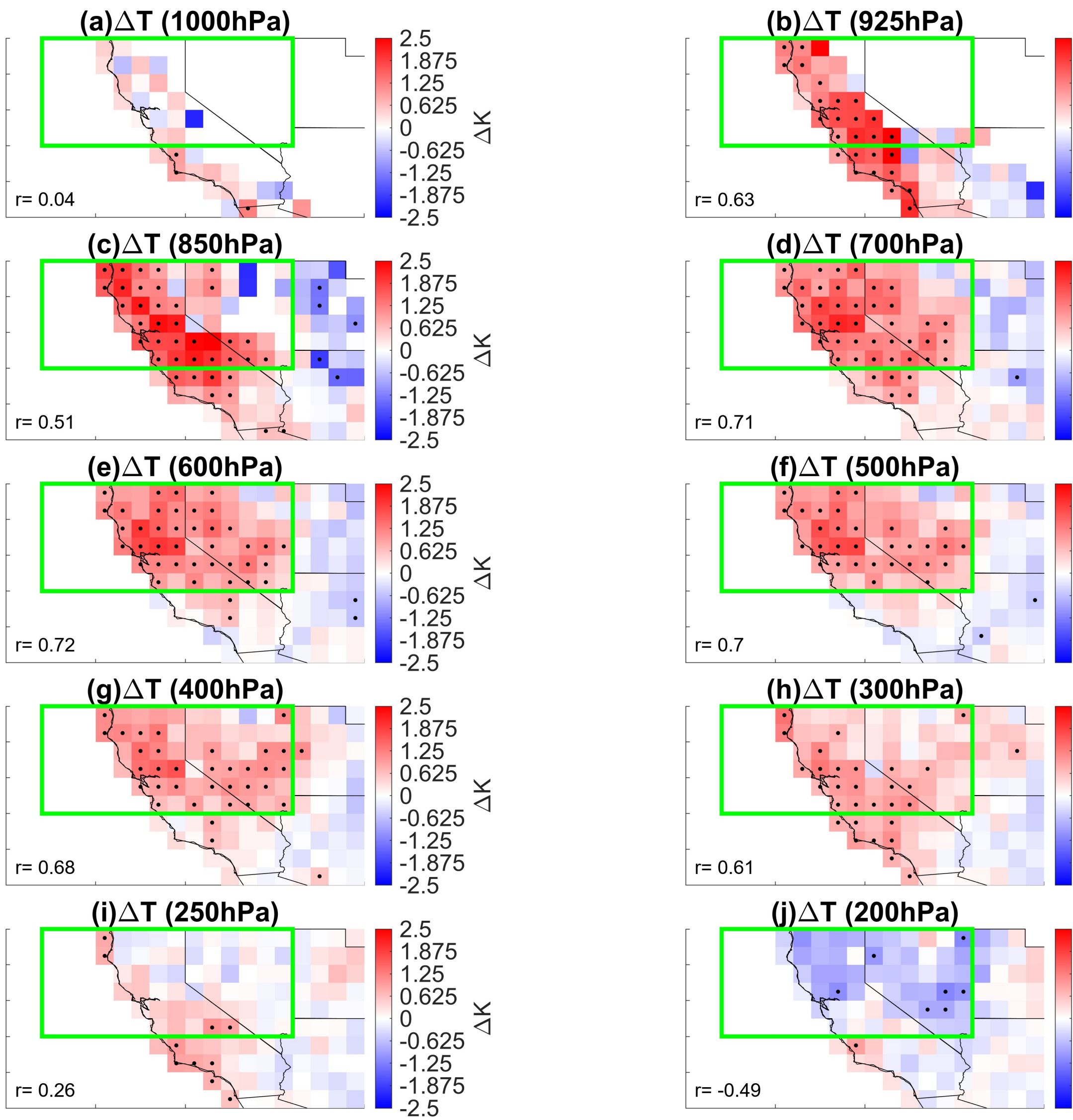

Figure 8. High minus low DM days AIRS T anomalies at all AIRS pressure levels from 1000 hPa to 200 hPa (a-j) under high RH_s conditions in the 2003-2022 June-October time period. Black dots indicate statistical significance at the 90% confidence interval. r values indicate spatial Pearson cross correlations between T and MODIS AOD.

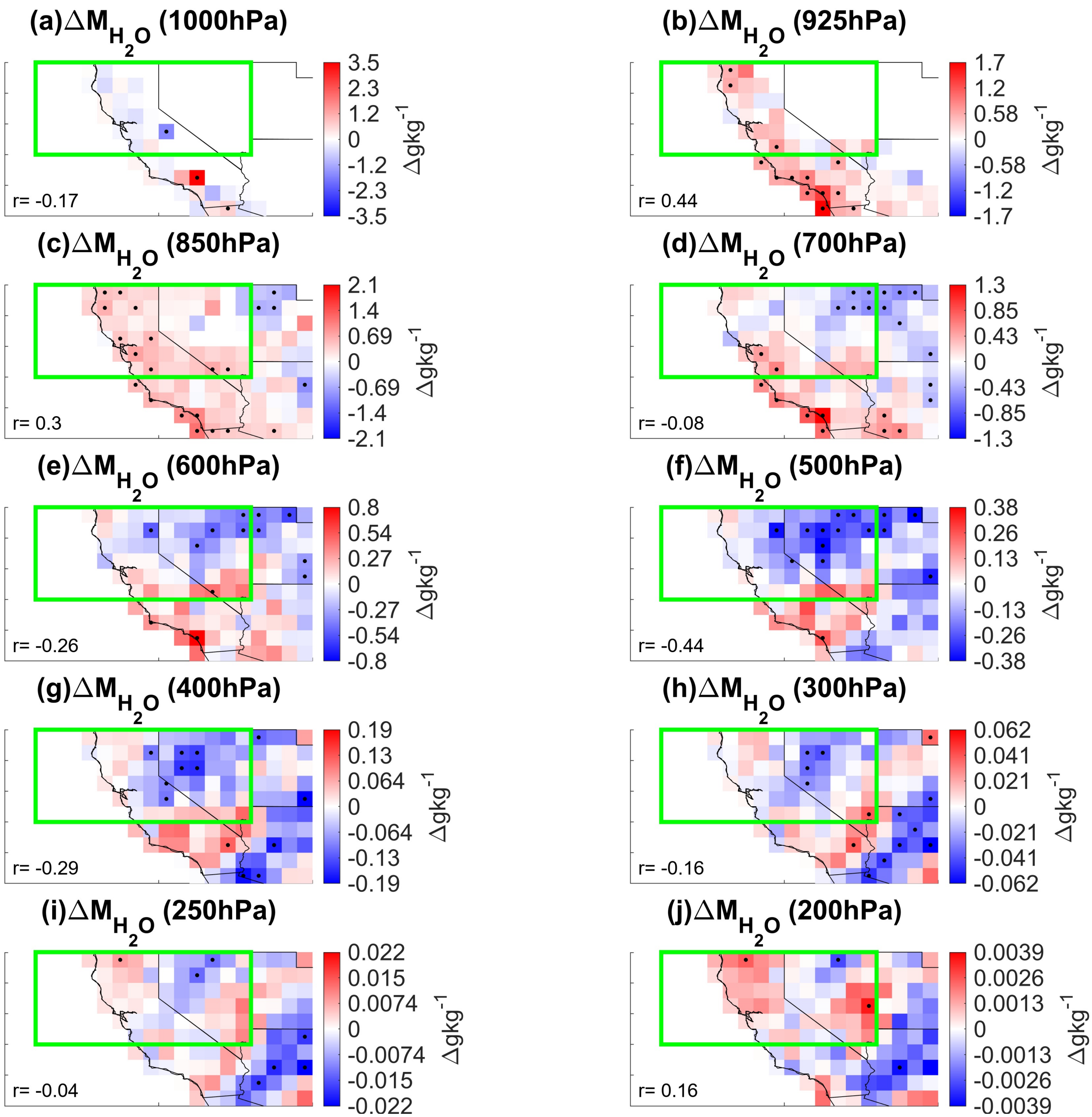

Figure 9. Effect size of large fires on the mean of various meteorological variables. 2003-2022 June-October Cohen's d d values for the difference between northern California-Nevada (nCA-NV) regional averages of variables on high (90th percentile) northern California (nCA) fire dry matter DM emission days and High minus low (10th percentile) nCA DM emission days that coincide with (a) high surface AIRS M_{H_2O} anomalies at all AIRS pressure p_s anomaly and levels from 1000 hPa to 200 hPa (ba-j) low p_s anomalyunder high RH_s conditions in the 2003-2022 June-October time period. Variables include liquid water cloud fraction CF_{lw}, cirrus cloud fraction CF_{cir}, cloud fraction CF, cloud top height CTH, precipitation, and top of atmosphere (TOA) shortwave (SW) fluxBlack dots indicate statistical significance at the 90% confidence interval. (a) represents r values of Cohen's d for 90th percentile surface pressure p_s days while (b) represents values of Cohen's d for 10th percentile p_s days. For Cohen's d, values of 0.2 through 0.5 signify a weak effect size, values of 0.5 through 0.8 represent a moderate effect size, indicate spatial Pearson cross correlations between total M_{H_2O} and values greater or equal to 0.8 signify a strong effect sizeMODIS AOD.Red bars represent standard error.

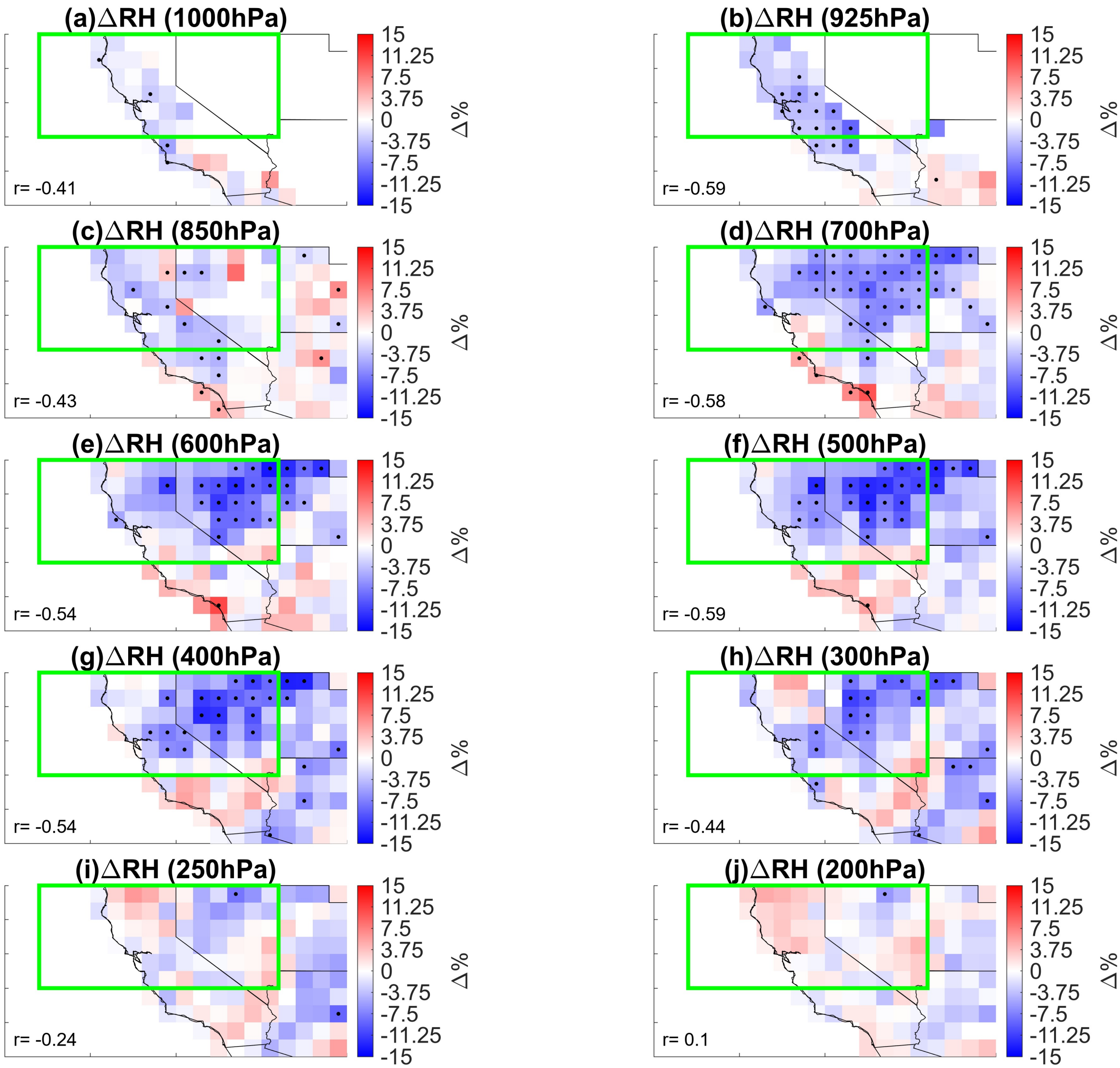

Figure 10. ~~Meteorological responses under high versus~~ High minus low ~~fire~~ DM days ~~with simultaneously low surface pressure. Difference between average variable~~ AIRS RH anomalies ~~on high~~ at all AIRS pressure levels from 1000 hPa to 200 hPa (~~90th percentile~~a-j) ~~northern California (nCA) fire dry matter DM emission days and low (10th percentile) nCA DM emission days that occur on low surface pressure p_s days~~ under high RH_s conditions in the 2003-2022 June-October time ~~frame~~period. ~~Variables include (a) 700hPa-250hPa average Temperature T_{ct}, 700hPa-250hPa average relative humidity RH_{ct}, (c) surface temperature T_s, (d) surface relative humidity RH_s, (e) cloud fraction CF, (f) cloud top height CTH, (g) precipitation, and (e) top of atmosphere TOA shortwave SW flux.~~ Black dots ~~represent statistically significant differences~~ indicate statistical significance at the 90% confidence interval~~according to a two tailed test~~. ~~Green box symbolizes the northern California-Nevada region. Pearson cross correlation~~ r values ~~in the top left corner of each plot represent the~~ indicate spatial ~~correlation~~ Pearson cross correlations between RH and MODIS ~~Deep Blue aerosol optical depth~~ AOD~~anomaly and the variable anomaly depicted in the figure~~.~~All values of r are significant at the 90% confidence interval according to a two-tailed test.~~

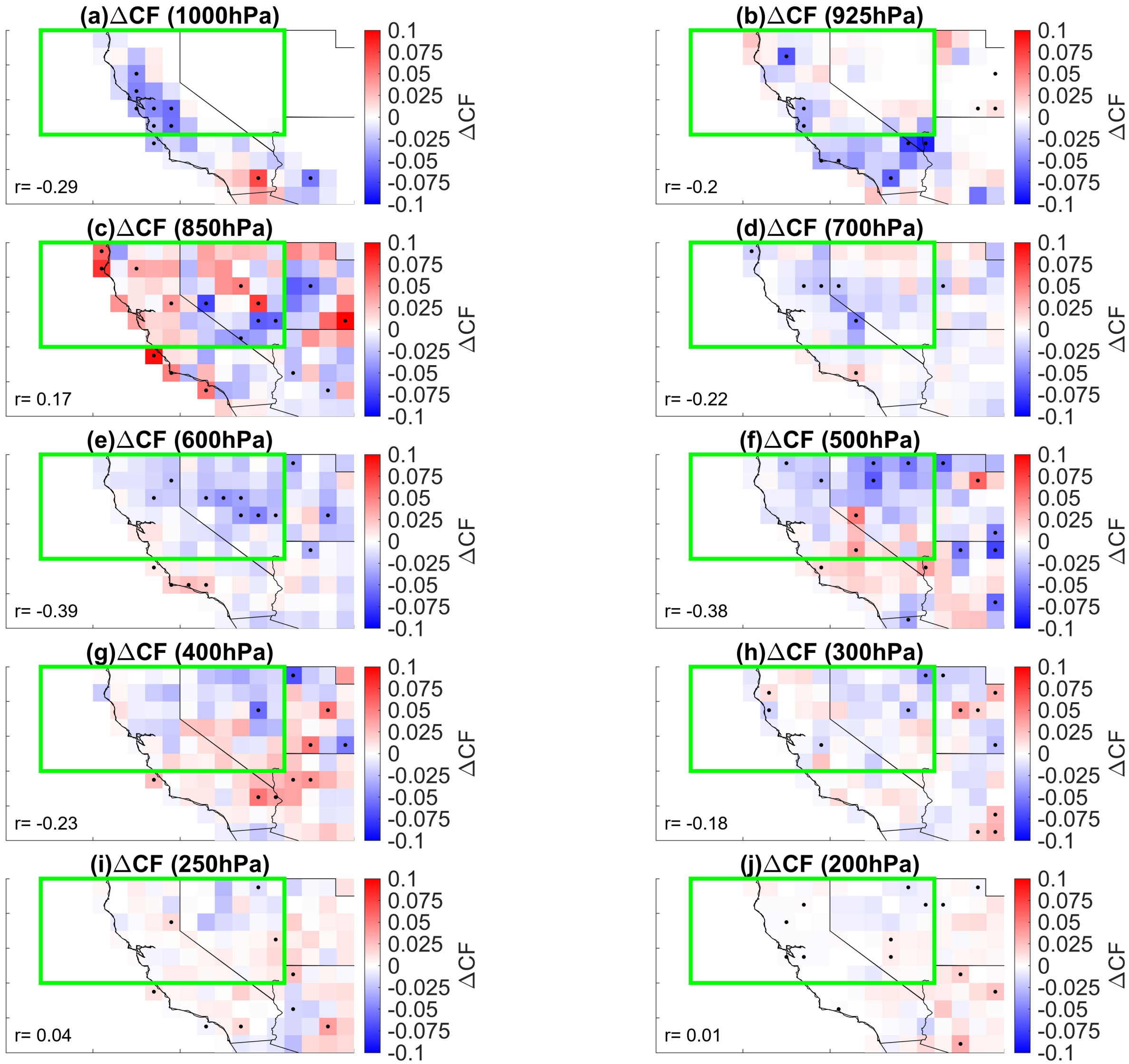

Figure 11. ~~Responses of liquid water and cirrus cloud fraction under high versus~~ High minus low ~~fire~~ DM days ~~with simultaneously low surface pressure. Difference between average variable~~ AIRS CF anomalies ~~on high~~ at all AIRS pressure levels from 1000 hPa to 200 hPa (~~90th percentile~~a-j) ~~northern California (nCA) fire dry matter DM emission days and low (10th percentile) nCA DM emission days that occur on low surface pressure p_s days~~ under high RH_s conditions in the 2003-2022 June-October ~~timeframe~~time period. ~~Variables include (a) liquid water cloud fraction CF_{lw} and (b) cirrus cloud fraction CF_{cir}.~~ Black dots ~~represent statistically significant differences~~ indicate statistical significance at the 90% confidence interval~~using a two-tailed test~~. r ~~represents~~ values indicate spatial Pearson cross ~~correlation coefficient values for cross~~ correlations between ~~aerosol optical depth~~ CF and ~~the variable of interest~~MODIS AOD.~~The green box represents the northern California-Nevada region. The spatial extent of the changes in CF_{cir} align with the changes in high troposphere water mass mixing ratio in **Figure 6a**, while the changes in CF_{lw} align more with the changes in low/mid troposphere temperature in Figure 6e.~~

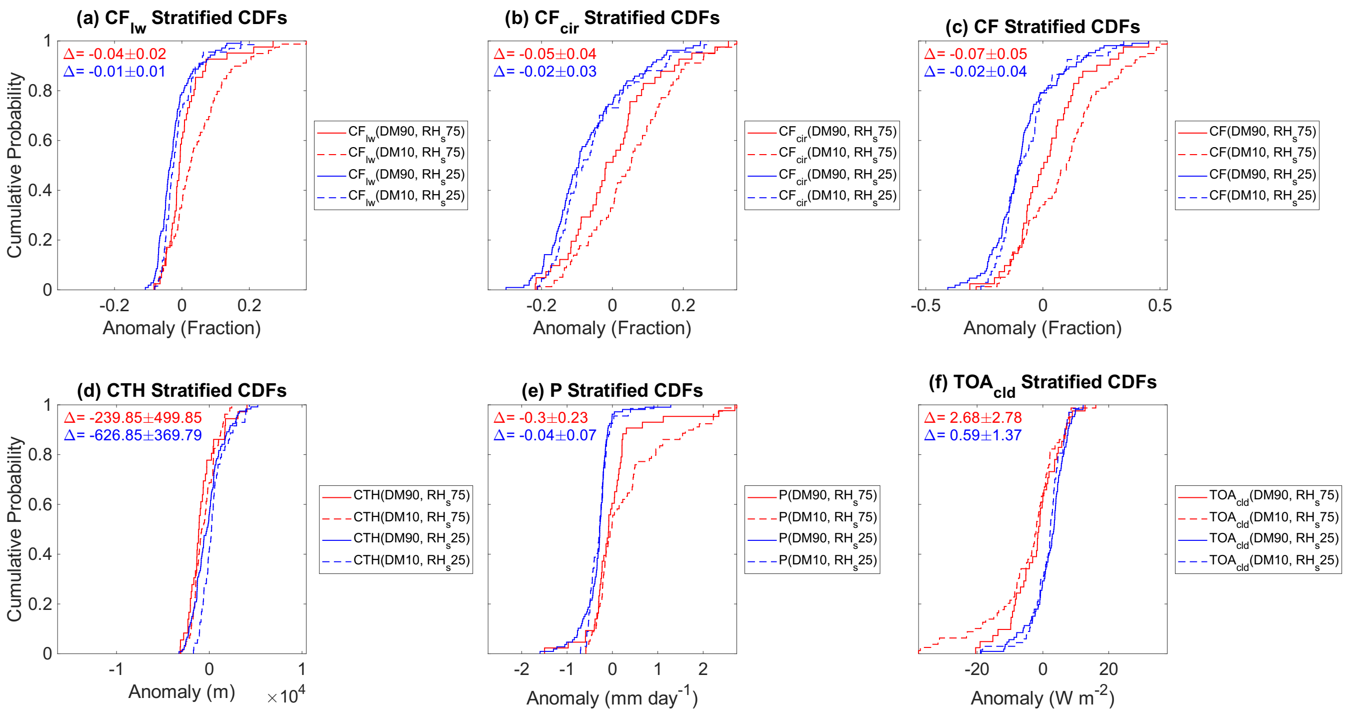

Figure 12. Dependence of microphysical meteorological variables to on high (90th percentile) versus low (10th percentile) surface pressure p_s RH_s and fires during the fire season. Cumulative distribution functions (Empirical CDFs) for cloud microphysical variables' regional average daily anomalies of meteorological variables over the northern California-Nevada (nCA-NV) region in the 2003-2022 June-October time frameperiod. Solid red line signifies variable anomalies are stratified by high northern California (nCA) fire dry matter emission DM and high surface pressure p_s nCA-NV RH_s anomaly days ($DM90, p_s90$$DM90, RH_s75$). The dashed red line signifies variable anomalies are stratified by low DM and high p_s RH_s anomaly days ($DM10, p_s90$$DM10, RH_s75$). The solid blue line represents variable anomalies are stratified by high DM and 10th percentile p_s low RH_s anomaly days ($DM90, p_s10$$DM90, RH_s25$). The dashed blue line symbolizes variable anomalies are stratified by low nCA DM and p_s RH_s anomaly days ($DM10, p_s10$$DM10, RH_s25$). Variables depicted include (a) liquid effective radius R_{eff}water cloud fraction CF_{lw}, (b) Ice R_{eff}cirrus cloud fraction CF_{cir}, (c) liquid water path $LWP$$CF$, (d)cloud top height CTH, (e) precipitation P, and ice water path IWPcloud-only (all-sky minus clear-sky) net top of atmosphere flux TOA_{cld}. The red Δ represents the differences in the mean of the solid red and dashed red lines ($DM90, p_s90$$DM90, RH_s75$)-($DM10, p_s90$$DM10, RH_s75$). The blue Δ represents the differences in the mean of the solid blue and dashed blue lines ($DM90, p_s10$$DM90, RH_s25$)-($DM10, p_s10$$DM10, RH_s25$).

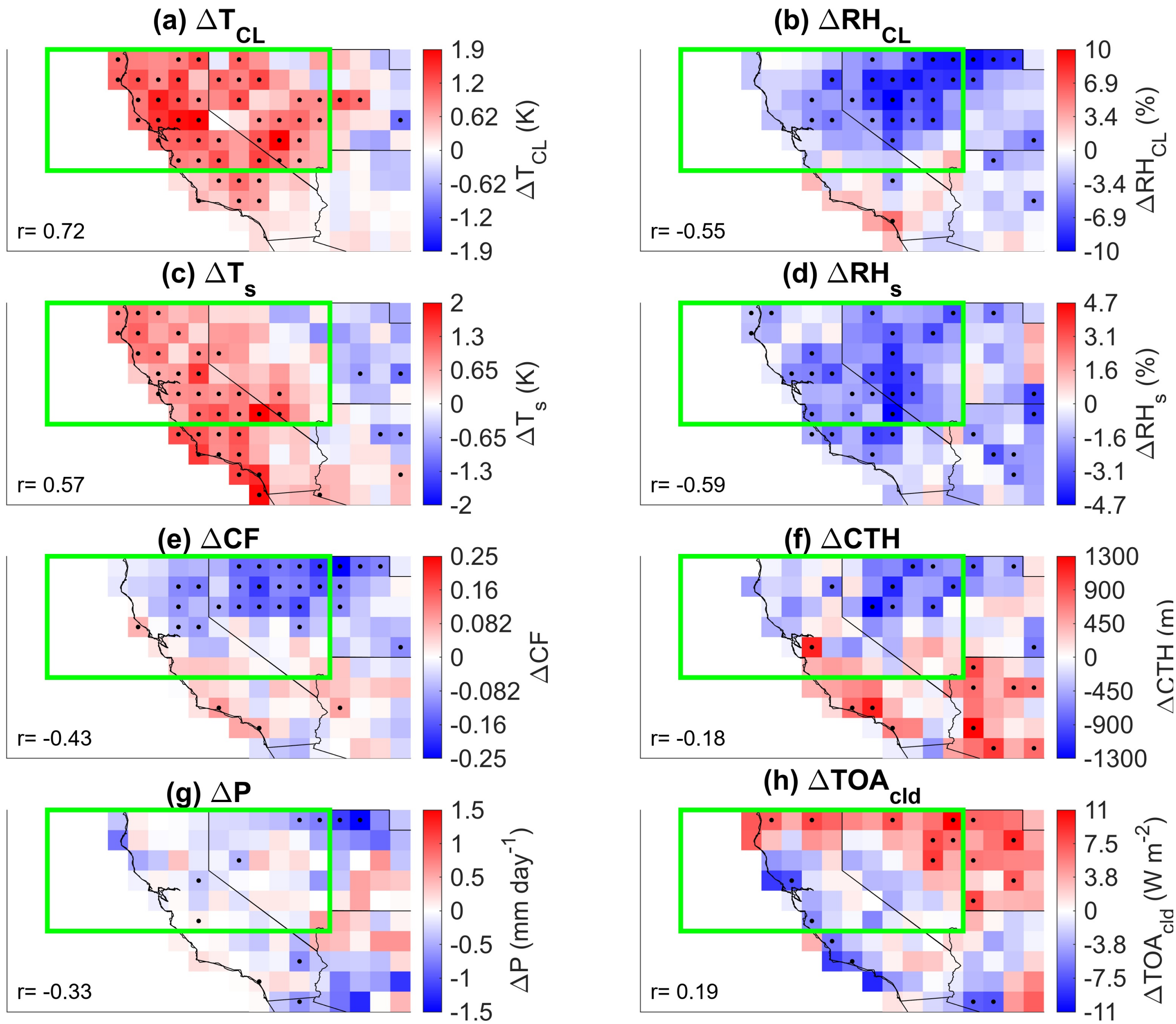

Figure 13. Meteorological responses under high versus low nCA DM conditions with simultaneously high nCA-NV RH_s during the fire season. Difference between average variable anomalies on high (90th percentile) nCA fire dry matter DM emission days and low (10th percentile) nCA DM emission days that occur on high nCA-NV RH_s days in the 2003-2022 June-October time period. Variables include (a) 850 hPa-300 hPa average Temperature T_{cl}, 850 hPa-300 hPa average relative humidity RH_{cl}, (c) surface temperature T_s, (d) RH_s, (e) CF, (f) CTH, (g) P, and (e) TOA_{cld} . Black dots represent statistically significant differences at the 90% confidence interval according to a two tailed test. Pearson cross correlation r values in each plot represent the spatial correlation between MODIS aerosol optical depth AOD anomaly and the variable anomaly depicted in the figure. All values of r are significant at the 90% confidence interval according to a two-tailed test.

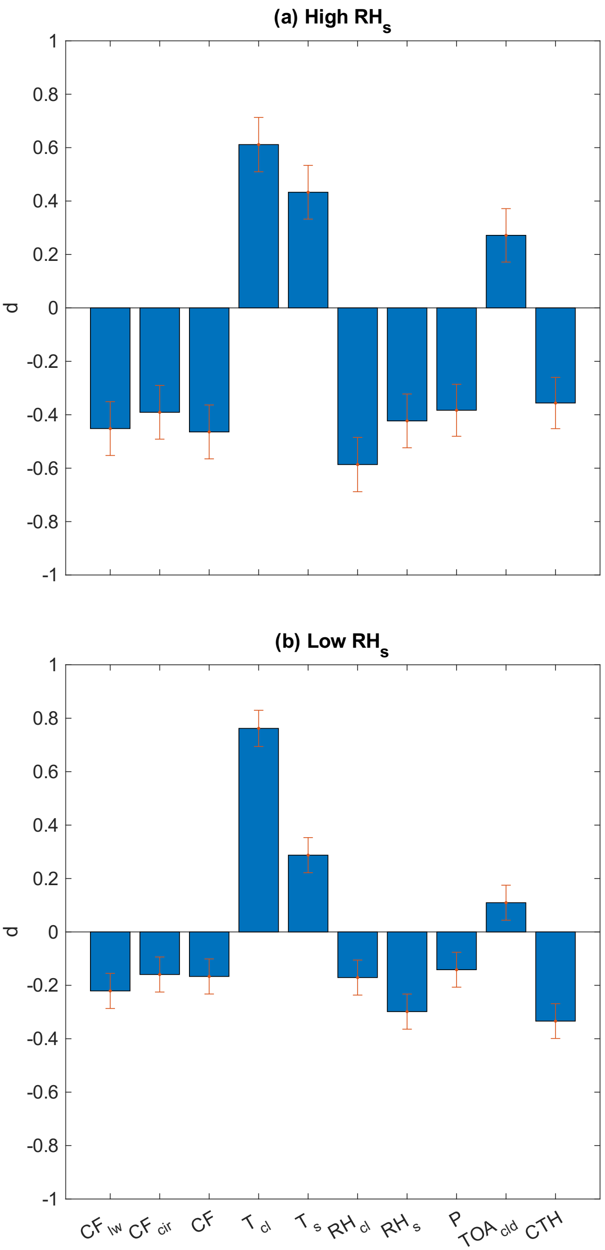

Figure 14. Effect size of large fires in nCA on the mean of various meteorological variables during the fire season. 2003-2022 June-October Cohen's d d values for the difference between nCA-NV regional averages of variables on high DM days minus low nCA DM emission days that coincide with (a) high RH_s and (b) low RH_s. For Cohen's d, values of 0.2 through 0.5 signify a weak effect size, values of 0.5 through 0.8 represent a moderate effect size, and values greater or equal to 0.8 signify a strong effect size. Red bars represent standard error.

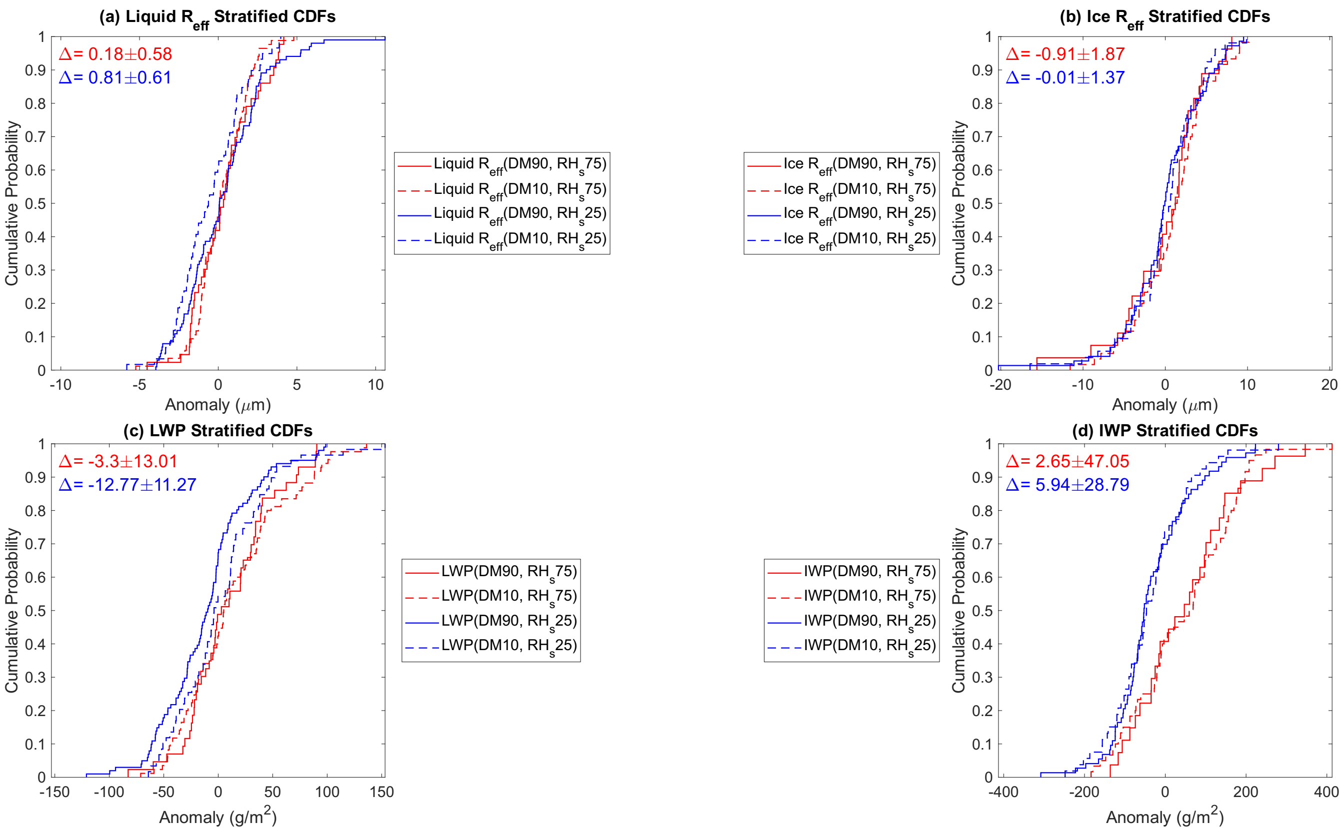

Figure 15. Dependence of microphysical variables to high versus low surface relative humidity RH_s and fires during the fire season. Empirical CDFs for regional average daily anomalies of cloud microphysical variables over the nCA-NV region in the 2003-2022 June-October time period. Solid red line signifies variable anomalies are stratified by ($DM90, RH_s75$). The dashed red line signifies variable anomalies are stratified by ($DM10, RH_s75$). The solid blue line represents variable anomalies are stratified ($DM90, RH_s25$). The dashed blue line symbolizes variable anomalies are stratified by ($DM10, RH_s25$). Variables depicted include (a) liquid effective radius R_{eff}, (b) Ice R_{eff}, (c) liquid water path LWP, (d) and ice water path IWP. The red Δ represents the differences in the mean of the solid red and dashed red lines ($DM90, RH_s75$)-($DM10, RH_s75$). The blue Δ represents the differences in the mean of the solid blue and dashed blue lines ($DM90, RH_s25$)-($DM10, RH_s25$).